

# Ultra-peripheral $J/\psi$ production in PbPb collisions at $\sqrt{s_{NN}}=2.76$ TeV with CMS

By

R. Patrick Kenny III

Submitted to the Department of People who read Abstracts and the  
Graduate Faculty of the University of Kansas  
in partial fulfillment of the requirements for the degree of  
Doctor of Philosophy

Committee members

---

MEMBER 1, Chairperson

---

MEMBER 2

---

MEMBER 3

---

MEMBER 4

Date defended: October 02, 2012

The Dissertation Committee for R. Patrick Kenny III certifies  
that this is the approved version of the following dissertation :

Ultra-peripheral  $J/\psi$  production in PbPb collisions at  $\sqrt{s_{NN}}=2.76$  TeV with CMS

---

MEMBER 1, Chairperson

Date approved: October 03, 2012

# Abstract

The first is some L<sup>A</sup>T<sub>E</sub>X code, don't change it.

## **Acknowledgements**

I would like to thank all of the little people who made this thesis possible.

# Contents

<b>1</b>	<b>Introduction</b>	<b>1</b>
1.1	Theoretical Context . . . . .	1
1.2	History . . . . .	1
<b>2</b>	<b>Theory</b>	<b>2</b>
2.1	Introduction . . . . .	2
2.2	QCD/QGP . . . . .	4
2.3	CGC/initial state . . . . .	4
2.4	Weizsäcker-Williams Approximation . . . . .	4
2.5	Vector Meson Dominance . . . . .	9
2.6	Leading Twist Approach Derivation . . . . .	14
2.7	Perturbative Quantum Chromo-dynamics . . . . .	17
2.8	Incoherent Photoproduction . . . . .	19
2.9	Photon Induced Nuclear Break-up . . . . .	19
2.10	Theoretical Results . . . . .	19
<b>3</b>	<b>The CMS Detector</b>	<b>23</b>
3.1	Trigger . . . . .	27
<b>4</b>	<b>Analysis</b>	<b>28</b>
4.1	MC Simulation . . . . .	28

4.2	Trigger Development . . . . .	29
4.2.1	L1 Trigger . . . . .	30
4.2.2	HLT Trigger . . . . .	31
4.3	Data Sets and Event Selection . . . . .	32
4.3.1	Data Set . . . . .	32
4.3.2	Event selection . . . . .	33
4.4	Break up determination . . . . .	35
4.4.1	ZDC Signal Reconstruction . . . . .	35
4.4.2	Determination of the one neutron thresholds . . . . .	36
4.5	Signal extraction . . . . .	39
4.6	Efficiency determination . . . . .	41
4.6.1	Muon Efficiencies . . . . .	41
<b>5</b>	<b>Results</b>	<b>45</b>
5.1	Coherent cross section . . . . .	45
5.2	Incoherent cross section . . . . .	45
5.3	Break up ratios . . . . .	45
5.4	diMuon-neutron correlations . . . . .	45
<b>6</b>	<b>Conclusion</b>	<b>54</b>
6.1	xsection results . . . . .	54
6.2	correlation results . . . . .	54
<b>7</b>	<b>Future Works</b>	<b>55</b>
7.1	Studies of 2011 PbPb data . . . . .	55
7.1.1	High mass $\gamma - \gamma \rightarrow e^+e^-$ in PbPb 2011 . . . . .	55
7.1.2	UPC Hadronic Overlap and PbPb 2011 . . . . .	56
7.1.3	UPC with muons in HF . . . . .	58
7.2	Studies of 2013 pPb data and 2015 PbPb data . . . . .	58

7.2.1	pPb $J/\psi$ . . . . .	59
7.2.2	UPC $J/\psi$ and $\Upsilon$ in 2015 . . . . .	59
7.2.3	UPC jets . . . . .	60
<b>A</b>	<b>My Appendix, Next to my Spleen</b>	<b>64</b>

# List of Figures

2.1	The electromagnetic field boosted and at rest. . . . .	4
2.2	The zero and first order modified Bessel functions. . . . .	7
2.3	AB is the pQCD method, RSZ-LTA is the LTA method, and STARlight is the VMD model. . . . .	20
2.4	Nuclear suppression factor, $S$ , in the pQCD and LTA methods. . . . .	21
2.5	Nuclear suppression factor, $S$ , in VMD method. . . . .	22
3.1	The Compact Muon Solenoid from Reference [1]. . . . .	24
3.2	The energy resolution of ECAL as a function of energy from Reference [1]. . . . .	25
3.3	The $E_T$ resolution of HCAL as a function of $ \eta $ and $E_T$ from Reference [1]. . . . .	26
4.1	Comparison of the of the dimuon rapidity distributions between coherent MC sample and Data. . . . .	28
4.2	Comparison of the of the dimuon $\phi$ distributions between coherent MC sample and Data. . . . .	29
4.3	Comparison of the of the dimuon $p_T$ distributions between coherent MC sample and Data. . . . .	30
4.4	ZDC pluse shape. . . . .	35
4.5	Comparison of ZDC signal reconstruction methods. . . . .	37
4.6	Effects of requiring in time signal in ZDC hadronic channels. . . . .	37
4.7	Effect of ZDC signal timing requirements after noise subtraction. . . . .	38



4.8	Fit to charge spectrum from $ZDC^-$ (left) and $ZDC^+$ (right) using method 1 . . . . .	38
4.9	Fit to charge spectrum from $ZDC^-$ (left) and $ZDC^+$ (right) using method 2 . . . . .	39
4.10	Mass fit to $J/\psi$ using Gaussian (Left) and Crystal Ball (Right) for the signal and a polynomial for the background . . . . .	40
4.11	Coherent, incoherent, and photon-photon process $p_T$ template fit to data. . . . .	40
4.12	Muon daughter detectability from coherent $J/\psi$ , incoherent $J/\psi$ , photon-photon, and $J/\psi$ gun samples. . . . .	42
4.13	Dimuon acceptance from coherent $J/\psi$ (top left), incoherent $J/\psi$ (top right), and photon-photon interactions (lower). . . . .	43
4.14	Fits to tag and probe pairs in the $J/\psi$ mass region. . . . .	44
4.15	Muon trigger efficiencies in $p_T$ and $\eta$ bins from the tag and probe method. . . . .	44
5.1	Invariant mass spectrum of the opposite signs di-muons originating from the co- herent $J/\psi$ for $X_n 0_n$ breakup mode for two invariant mass regions. . . . .	46
5.2	Invariant mass spectrum of the opposite signs di-muons originating from the inco- herent $J/\psi$ for $X_n 0_n$ breakup mode for two invariant mass regions. . . . .	46
5.3	Ratio between $J/\psi$ yields $X_n X_n$ and $1n 0_n$ break-up modes compared the $X_n 0_n$ break-up mode for $J/\psi$ with $p_T$ below 150 MeV. . . . .	47
5.4	Ratio between $J/\psi$ yields $X_n X_n$ and $1n 0_n$ break-up modes compared the $X_n 0_n$ break-up mode for $J/\psi$ with $0.2 < p_T < 1.5$ GeV. . . . .	48
5.5	Transverse momentum distribution of the $J/\psi$ when $J/\psi$ and neutron have the same or opposite rapidity direction from data (left) and from theory (right). . . . .	49
5.6	Ratio between the transverse momentum distribution of the $J/\psi$ when $J/\psi$ and neutron have the opposite direction and the transverse momentum distribution of the $J/\psi$ when $J/\psi$ and neutron have the same direction. . . . .	49
5.7	The rapidity distribution of the coherent (top) and incoherent (bottom) $J/\psi$ for the $ZDC^+$ and $ZDC^-$ . . . . .	52

5.8	The rapidity distribution of the coherent (left) and incoherent (right) $J/\psi$ for the ZDC <sup>+</sup> and ZDC <sup>-</sup> from MC (particle gun with customized $J/\psi p_T$ input distribution).	53
7.1	Coherent excess in inclusive $J/\psi p_T$ spectrum.	57

# List of Tables

2.1	$\sigma_{AA \rightarrow AAJ/\psi}(mb)$ the LTA, VMD, pQCD methods. Four different gluon density models are used in the pQCD method. STARlight is a simulation software package that utilizes the VMD model. . . . .	20
4.1	List of 2011 L1 seeds. . . . .	31
4.2	List of 2011 HLT trigger. . . . .	31
4.3	Integrated luminosities and number of events for the three samples used in this analysis. . . . .	33
5.1	Number of coherent $J/\psi$ integrated over $p_T$ and $y$ with statistical uncertainty. . . .	47
5.2	Number of coherent $J/\psi$ integrated over $p_T$ and $y$ with statistical uncertainty. . . .	47
5.3	Number of $J/\psi$ integrated over $p_T$ and $y$ with statistical uncertainty. . . . .	48
5.4	Final number of $J/\psi$ (for both ZDCs and for two negative and positive rapidity) and ratios with statistical uncertainty. . . . .	50

# **Chapter 1**

## **Introduction**

### **1.1 Theoretical Context**

### **1.2 History**

# Chapter 2

## Theory

### 2.1 Introduction

Microseconds after the big bang, the universe existed in a state known as the Quark Gluon Plasma (QGP). In the QGP, quarks and gluons are not in hadronic bondage, forced to the confines of bound states such as protons and neutrons. The Large Hadron Collider (LHC) produces QGP in the lab in PbPb (lead-lead) collisions. The high energies and rates of the collisions at the LHC make it possible to do detailed studies of the QGP. The LHC is producing rare experimental probes such as suppressed jets and heavy quarkonia at an unprecedented rate in heavy-ion collisions. Physicists now have better constraints on the properties like temperature, viscosity, and energy density of the QGP.

The detailed studies of PbPb collisions coming out of the LHC experiments require an understanding of the initial state of the ions before they collide. Without knowledge of the initial state, physicists cannot determine which experimental effects are due to the QGP and which effects are inherent to the nuclei themselves. For example, suppression of heavy quarkonia is a signature of the QGP but also appears to occur in deuterium-gold collisions where the QGP is not expected to arise [2]. Because it is not certain how much of the reduction of quarkonia production is due to the initial state of the nuclei, the reduction due to the QGP is unclear. Without a clean probe of the

initial state, physicists' knowledge of the QGP is limited. Ultra-Peripheral Collisions (UPC) at the LHC fill this need for a clean probe.

The colliding nuclei interact electromagnetically in an UPC event, avoiding the complicated mixing of final state and initial state effects found in nuclear collisions. In UPC events, no QGP state emerges, and the effects arising from the QGP no longer obscure the initial state effects. Other initial state probes such as peripheral nuclear collisions and proton-nucleus collisions have the potential to create the QGP obscuring which effects come from the initial state. It is impossible to create the QGP in UPC events because the nucleons within the nucleus do not collide. UPC events provide clarity by enhancing physicists' understanding of the initial state.

The interactions between the field of photons surrounding the colliding nuclei and the gluons of nuclei can produce a  $J/\psi$  probing the gluon density. The UPC  $J/\psi$  photoproduction cross section is therefore a probe of the initial state of the nucleus. The Weizsäcker-Williams approximation provides a way to calculate the density of probing photons that surrounds the nucleus. The electron-proton scattering data gives a value for the proton photoproduction cross section at lower energies. The perturbative Quantum Chromo-dynamics (pQCD), Vector Meson Dominance (VMD), and Leading Twist (LTA) methods all combined the nuclear photon flux with the proton scattering data to calculate the nuclear photoproduction cross section. Each of these methods handle the gluon density of the nucleus differently producing a measurable difference in the value of the  $J/\psi$  photoproduction cross section.

## 2.2 QCD/QGP

## 2.3 CGC/intial state

## 2.4 Weizsäcker-Williams Approximation

The Weizsäcker-Williams approximation relates the electric field of a stationary point charge to the photon field that arises at ultra relativistic velocities. The approximation is semi-classical and combines both classical and quantum elements. A Fourier transform of Maxwell's equations combine with Einstein's equation for the energy of a photon in the Weizsäcker-Williams approximation.

The frequency modes of the electrostatic field are treated as photons. The conversion of the electric field to a flux of photons simplifies the calculation of interaction cross sections. The Weizsäcker-Williams approximation makes the calculation of electromagnetic interactions with the nucleus tractable.

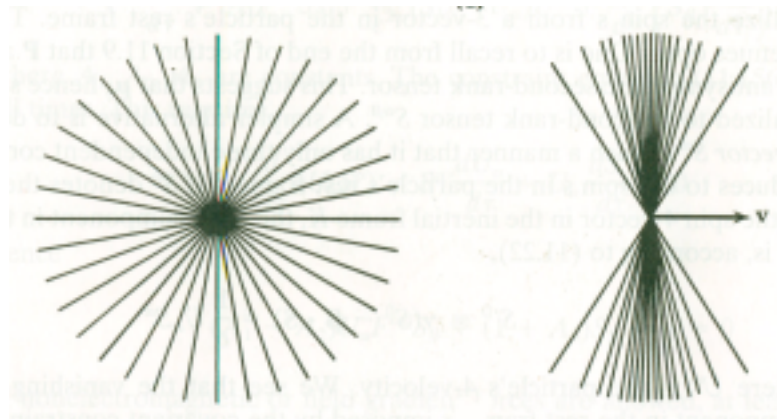


Figure 2.1: The electromagnetic field boosted and at rest.

The Weizsäcker-Williams approximation begins with the equation for the electric field of the projectile nucleus at rest. The electromagnetic field only needs to be considered at the position of the target nucleus. From the projectile's point of view, the target is moving and contributes  $-vt$  to

Eq. 2.1, the equation for the electric field of the projectile nucleus at rest.

$$x' = -vt' \quad y' = b \quad z' = 0 \quad \vec{\mathbf{E}}' = \left( \frac{eZ}{4\pi\epsilon_0 \left( (-vt')^2 + b^2 \right)^{3/2}} \right) \left( -vt' \hat{\mathbf{x}}' + b \hat{\mathbf{y}}' \right) \quad (2.1)$$

In Eq. 2.1,  $b$  is the impact parameter, the distance of separation at closest approach,  $v$  is the velocity of the projectile nucleus,  $Z$  is the number of protons in the nucleus, and  $e$  is the charge of the electron. Two simplifications occur due to the coordinates of Eq. 2.1. The magnetic field is equal to zero, because the projectile is at rest, and the  $z$  coordinate can be ignored, reducing the equation to two dimensions.

The Lorentz transformation converts the field equations in the projectile's frame to equations in the target's frame. The result is a set of equations that relate the electric and magnetic field components in one frame to the components of the electric and magnetic field in another frame moving at a different constant velocity. Eq. 2.2 gives the result of the transformation from the projectile's primed frame to the target's rest frame for the field components [3]:

$$\begin{aligned} E'_x &= E_x & \gamma(E'_y/c + \beta B'_z) &= E_y/c & \gamma(E'_z/c + \beta B'_y) &= E_z/c \\ B'_x &= B_x & \gamma(B'_y - \beta E'_z/c) &= B_y & \gamma(B'_z + \beta E'_y/c) &= B_z \end{aligned} \quad (2.2)$$

The transformation equations for the fields, Eq. 2.2, and the transformation of the coordinates reduce to Eq. 2.3 [3]:

$$\begin{aligned} E'_x &= E_x & \gamma E'_y &= E_y & \gamma \beta E'_y/c &= B_z \\ ct' &= \gamma ct & x' &= -\gamma \beta ct \end{aligned} \quad (2.3)$$

The simplicity of Eq. 2.1 creates the simplicity of Eq. 2.2. The Lorentz transformation reduces the six components of the electromagnetic field in the target's frame to the three equations in Eq. 2.2 by relating them to the fields of the projectile's frame.



The combination of Eq. 2.1 and Eq. 2.2 produce equations for the electric and magnetic fields in the target's rest frame. Eq. 2.1 gives the expression for the field components as seen in the projectile frame.

$$\begin{aligned}\vec{\mathbf{E}} &= \left( \frac{\gamma e Z}{4\pi\epsilon_0 \left( (\gamma vt)^2 + b^2 \right)^{3/2}} \right) (vt\hat{\mathbf{x}} + b\hat{\mathbf{y}}) \\ \vec{\mathbf{B}} &= \frac{\gamma\beta e Z b}{4\pi c\epsilon_0 \left( (\gamma vt)^2 + b^2 \right)^{3/2}} \hat{\mathbf{z}} = \frac{\gamma\mu_0 v e Z b}{4\pi \left( (\gamma vt)^2 + b^2 \right)^{3/2}} \hat{\mathbf{z}}\end{aligned}\quad (2.4)$$

If the impact parameter  $b$  goes to zero, the target sits in the line of the projectile particle's motion, and the denominator carries a factor of  $\gamma$  squared. If  $vt$  goes to zero, the projectile particle is directly above or below in the  $y$  direction, and the numerator carries a factor of  $\gamma$ . This results in fields that are a factor of  $\gamma^3$  higher in the  $y$  direction than in the  $x$  direction (see Fig. 2.1). The boost compresses the electric field of the charge in the direction of the boost and produces a magnetic field resulting in a form similar to radiation. The point charge at ultra relativistic velocities produces a strong electric field in the plane transverse to its motion resembling a plane wave.

Separating the even and odd functions of the electromagnetic field simplify the decomposition of the field equations into Fourier modes. The even functions decompose into cosine functions, odd functions into sine functions. The  $y$ -component of the electric field and the  $z$ -component of the magnetic field are even functions in time, and the  $x$ -component of the electric field is an odd function in time. Eq. 2.5 gives the Fourier transformation integrals.

$$\begin{aligned}E_x(\omega) &= \sqrt{\frac{2}{\pi}} \frac{eZ}{4\pi\epsilon_0 b^2} \int_0^\infty \frac{(\gamma vt/b) \sin(\omega t)}{\left( (\gamma vt/b)^2 + 1 \right)^{3/2}} dt & E_y(\omega) &= \sqrt{\frac{2}{\pi}} \frac{\gamma e Z}{4\pi\epsilon_0 b^2} \int_0^\infty \frac{\cos(\omega t)}{\left( (\gamma vt/b)^2 + 1 \right)^{3/2}} dt \\ B_z(\omega) &= \frac{\beta E_y(\omega)}{c}\end{aligned}\quad (2.5)$$

With the appropriate substitutions, tables provide solutions to the integrals of Eq. 2.5 as seen in

Ref. [4].

$$u = \frac{\gamma v t}{b} \quad du \left( \frac{b}{\gamma v} \right) = dt \quad \omega' = \frac{\omega b}{\gamma v}$$

$$\int_0^\infty \frac{u \sin(\omega' u)}{(u^2 + 1)^{3/2}} du = \omega' K_0(\omega') \quad \int_0^\infty \frac{\cos(\omega' u)}{(u^2 + 1)^{3/2}} du = \omega' K_1(\omega') \quad (2.6)$$

The Fourier transformation replaces the time variable with a frequency variable in the field equations. The frequency relates to photon energy by the Einstein's photon energy equation,  $E = \hbar \omega$ . The substitution of time with frequency allows for a flux of photons to replace the classical electromagnetic field.

The  $\gamma$  dependence of the field components is different because of the different  $t$  dependence of Eq. 2.6. The integrals in Eq. 2.6 shift the  $\gamma$  dependence of the field component equations. Eq. 2.7 gives the result of the integrals:

$$E_x(\omega) = \sqrt{\frac{2}{\pi}} \frac{eZ}{4\pi\epsilon_0 b^2} \frac{b}{\gamma v} \frac{\omega b}{\gamma v} K_0\left(\frac{\omega b}{\gamma v}\right) \quad E_y(\omega) = \sqrt{\frac{2}{\pi}} \frac{\gamma eZ}{4\pi\epsilon_0 b^2} \frac{b}{\gamma v} \frac{\omega b}{\gamma v} K_1\left(\frac{\omega b}{\gamma v}\right) \quad (2.7)$$

$\gamma$  is subsumed into the substitution from  $t$  to  $\omega$  in the numerator of the x-component and becomes a part of the zeroth-order modified Bessel function upon integration. The y-component does not have a factor of  $t$  in the numerator, therefore the factor of  $\gamma$  remains outside of the integral, and it does not get subsumed into the first-order modified Bessel function. In Eq. 2.7,  $E_y$  carries an additional factor of  $\gamma$  in the numerator relative to the  $E_x$ .  $E_y$  is  $\gamma$  times larger than  $E_x$ .

In the ultra-relativistic limit, the electric and magnetic fields have the same configuration as electromagnetic plane wave radiation. The electric and magnetic fields are perpendicular and related by a factor of  $c$  in the ultra rel-

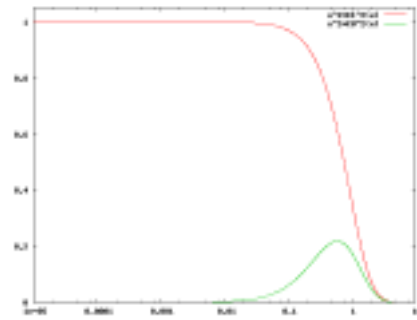


Figure 2.2: The zero and first order modified Bessel functions.

ativistic limit. When  $v$  approaches  $c$ ,  $\beta \approx 1$ , the y-component of the electric field and the z-component of the magnetic field are related by a factor of  $c$ ,  $E_y/c = B_z$ . Because  $K_0(x)$  is smaller than  $K_1(x)$  for all  $x$ , when  $\gamma \gg 1$ ,  $E_y$  is approximately equally to  $\gamma E_x$ . The conditions imposed by the ultra-relativistic limit result in the relationship of Eq. 2.8.

$$\gamma \gg 1 \rightarrow \gamma E_x \gg E_x \rightarrow E_y \gg E_x \quad (2.8)$$

The x-component of the electric field can therefore be ignored and the magnetic and electric fields are left perpendicular to each other. The six field components reduced to one electric component and one perpendicular magnetic field component, which have a configuration identical to a plane wave.

As with plane waves, the energy per area per time transfered by the electromagnetic field is given by the Poynting vector. The Poynting vector takes the simple form of a plane pulse propagating in the x direction.

$$\vec{S} \equiv \vec{E} \times \vec{B} / \mu_0 = (E_y^2 / c \mu_0) \hat{x} = c \epsilon_0 E_y^2 \hat{x} \quad (2.9)$$

The Poynting vector relates to the fluence (energy per unit area) [5],

$$I(b) = \hat{x} \cdot \int_0^\infty \vec{S} d\omega = \int_0^\infty (c \epsilon_0 E_y^2) d\omega = \int_0^\infty \left( \frac{dI}{d\omega} \right) d\omega \quad (2.10)$$

and the spectral fluence (energy per area per frequency).

$$\frac{dI}{d\omega} = c \epsilon_0 E_y^2 = \frac{e^2 Z^2 c}{4 \pi^3 b^2 v^2 \epsilon_0} \left( \frac{\omega b}{\gamma v} \right)^2 K_1^2 \left( \frac{\omega b}{\gamma v} \right) = \alpha \hbar \left( \frac{Z}{b \beta \pi} \right)^2 \left( \frac{\omega b}{\gamma v} \right)^2 K_1^2 \left( \frac{\omega b}{\gamma v} \right) \quad (2.11)$$

Substituting Eq. 2.7 into Eq. 2.10 gives the Poynting vector as a function of frequency. Eq. 2.11 paves the way for Einstein's equation. The spectral fluence given by Eq. 2.11 relates the frequency

to energy, which are the same quantities present in Einstein's equation.

Einstein's equation,  $E = \hbar\omega$ , gives the energy of a photon, which is related to the spectral fluence. If the fluence is due to a photon number density,  $N$ , Einstein's equation relates  $N$  to the fluence. The relationship between the number of photons per unit area in an infinitesimal energy range and the spectral fluence in an infinitesimal frequency range is given by Eq. 2.12 [3].

$$\frac{dI}{d\omega}d\omega = \hbar\omega N(\omega)d(\hbar\omega) \rightarrow \frac{1}{\hbar^2\omega} \frac{dI}{d\omega} = N(\omega) \quad (2.12)$$

Plugging Eq. 2.11 into Eq. 2.12 yields the semiclassical photon flux of an ultra-relativistic nucleus.

$$N(\omega, b) = \frac{\alpha}{\hbar\omega} \left( \frac{Z}{b\beta\pi} \right)^2 \left( \frac{\omega b}{\gamma v} \right)^2 K_1^2 \left( \frac{\omega b}{\gamma v} \right) \quad (2.13)$$

Eq. 2.13 replaces the classical electric field of a point charge with a semiclassical field of photons. Physicists can calculate the electromagnetic interactions between nuclei with the final result of the Weizsäcker-Williams approximation, Eq. 2.13. The photon flux in Eq. 2.13 provides the electromagnetic input to the  $J/\psi$  photoproduction cross section calculation.

## 2.5 Vector Meson Dominance

The Vector Meson Dominance method for calculating the  $J/\psi$  photoproduction cross section has three main components. VMD approach is constructed from the Weizsäcker-Williams photon flux, the VMD fit to the proton-electron data, and the Glauber model for calculating the nuclear cross sections from the proton-electron cross sections. The Weizsäcker-Williams photon flux provides the probe. The proton-electron scattering data combine with the Glauber model create a picture of the initial state of the nucleus. Each of the different approaches to calculating the UPC  $J/\psi$  photoproduction cross section use these same elements. However, the different models each use the last two elements differently to produce different pictures of the nucleus and different cross sections values.

The photon flux in the photoproduction cross section calculation must be finite in order for the cross section to be meaningful. The Weizsäcker-Williams approximation, Eq. 2.13, produces a divergence at  $b = 0$ . The probability of the nuclei interacting would exceed one if the photon flux were infinite. The divergence that arises at  $b = 0$  from  $K_1$  results in an unphysically infinite photon flux. Removing the divergence is necessary. Special treatment of impact parameter,  $b$ , where the colliding nuclei overlap eliminates the divergence.

A modulation of the photon flux can subdue the divergence at  $b = 0$ . A convolution of the photon flux with the nucleon number density functions of the colliding nuclei produces the necessary modulation. Eq. 2.14 gives the nucleon density of a single nucleus,

$$\rho_A(s) = \frac{\rho_0}{1 + \exp[(s - R_{WS})/d]} \quad (2.14)$$

In Eq. 2.14,  $s$  is the distance from the center of the nucleus,  $R_{WS}$  is the radius of the nucleus, and  $d$  is the skin depth, which determines how quickly the nucleon density falls off beyond the nuclear radius. In Eq. 2.15 the depth of the nucleus is integrated out leaving just the transverse dimension in  $T_A$ . The average number of nucleons in the overlap region is given by a convolution of  $T_A$  from each of the two nuclei to produce  $T_{AA}$ .

$$\begin{aligned} T_A(\vec{r}) &= \int dz \rho_A(\sqrt{|\vec{r}|^2 + z^2}) \\ T_{AA}(|\vec{b}|) &= \int d^2\vec{r} T_A(\vec{r}) T_A(\vec{r} - \vec{b}) \end{aligned} \quad (2.15)$$

$T_{AA}$  is the function that modulates the photon flux. As input to the Poisson distribution,  $T_{AA}$  reduces Eq. 2.13 at values of  $b$  where the nuclei overlap significantly and eliminates the divergence in the photon flux.

Modulating the photon flux by the probability that no nucleon-nucleon collisions occur limits the photon flux at low  $b$  in Eq. 2.13. The convolution of the photon flux with the  $b$  dependent probability that no nucleon-nucleon collisions occur removes the divergence in Eq. 2.13. Using the mean number of nucleons in the overlap region given by  $T_{AA}$ , the Poisson distribution gives the

probability that no collisions occur at a given  $b$ :

$$P_0(b) = \exp[-T_{AA}(b)\sigma_{NN}] \quad (2.16)$$

In Eq. 2.16,  $\sigma_{NN}$  is the cross section for a nucleon-nucleon interaction, which gives the probability that a collision will occur given the average number of nucleons in the overlap region. The average photon flux over impact parameter,  $b$ , can be calculated from the integration of the  $b$ -dependent photon flux, Eq. 2.13, with the  $b$ -dependent probability of having no nucleon-nucleon interactions, Eq. 2.16.

$$\frac{dN_\gamma(k)}{dk} = \int_0^\infty 2\pi b db P_0(b) \int_0^R \frac{r dr}{\pi R_A^2} \int_0^{2\pi} d\phi \frac{d^3N_\gamma(k, b + r \cos(\phi))}{dk d^2r} \quad (2.17)$$

Eq. 2.17 goes down to  $b = 0$  where the photon flux is infinite, but because the probability of having a nucleon-nucleon collisions is high, the divergence is eliminated. The result of Eq. 2.17 does not diverge.

A power-law fit to the proton photoproduction data gives an analytic expression for the energy dependence of the proton photoproduction cross section. The fitting function is simple and only depends on the photon-proton center of mass energy,  $W$ . Eq. 2.18 gives the parameterization of the forward proton photoproduction cross section fit.

$$\left. \frac{d\sigma(\gamma p \rightarrow V p)}{dt} \right|_{t=0} = b_v(XW^\epsilon + YW^{-\eta}) \quad (2.18)$$

$W$  is the center of mass energy of the proton-photon system in Eq. 2.18. The remaining variables in Eq. 2.18 are simple power-law fit parameters. The  $XW^\epsilon$  term characterizes pomeron mediated interactions, and the  $YW^{-\eta}$  term characterizes meson mediated interactions[6].  $J/\psi$ 's high mass relative to the  $\pi$  and  $\rho$  renders the second term in Eq. 2.18 negligible as the term falls rapidly with increasing  $W$ . Eq. 2.18 allows for extrapolation and interpolation of the measured forward proton photoproduction cross section. The fit to the data provides estimates for energies that have not yet been probed experimentally.

The proton-electron scattering data is used differently in the VMD method than in the other major methods. The VMD method for calculating UPC photoproduction cross sections relies more on electron-proton scattering data. The proton photoproduction cross sections from the electron-proton scattering data is a direct input to the VMD model. A power-law fit to the proton photoproduction data, as opposed to model dependent gluon densities of other approaches, combines with the Glauber model to provide the nuclear model in the VMD method. Because of the simplicity of the method, the VMD approach incorporates less modifications of the nuclear initial state relative to the proton initial state. As a result, the VMD method produces a higher UPC  $J/\psi$  photoproduction cross section relative to the other methods.

Vector meson dominance and the optical theorem allow for the calculation of the total proton-meson scattering cross section from the fit given by Eq. 2.18. The optical theorem relates a total cross section,  $\sigma$ , to a corresponding forward scattering cross section,  $d\sigma/dt|_{t=0}$ . Vector meson dominance asserts that the colored part of the photon wave function is dominated by vector mesons; therefore, the photon is represented as a quark-antiquark pair in photoproduction calculations. These two components combine to produce Eq. 2.19.

$$\begin{aligned} \frac{d\sigma(\gamma p \rightarrow Vp)}{dt} \Big|_{t=0} &= \frac{4\pi\alpha}{f_V^2(M_V, \Gamma_{l+l-})} \frac{d\sigma(Vp \rightarrow Vp)}{dt} \Big|_{t=0} \\ \sigma(Vp)_{tot}^2 &= 16\pi \frac{d\sigma(Vp \rightarrow Vp)}{dt} \Big|_{t=0} \end{aligned} \quad (2.19)$$

In Eq. 2.19, the photon-proton scattering is related to meson-proton scattering through the photon-meson coupling, which depends on the vector meson's mass,  $M_V$ , and leptonic decay width,  $\Gamma_{l+l-}$ . The result of combining vector meson dominance and the optical theorem in Eq. 2.19 provides the cross section for a meson to scatter off a proton. The total proton-meson scattering cross section, provides the input to the Glauber model calculation of the nuclear photoproduction cross section.

The nucleus-meson scattering cross section relates to Eq. 2.19 through the Glauber model. The Glauber model allows for Eq. 2.19, the proton-meson scattering cross section, to be used to calculate a nucleus-meson scattering cross section. The Glauber model produces nuclear cross

section calculations from nucleon (proton or neutron) interaction cross sections by use of  $T_{AA}$ . The combination of the mean number of nucleons in the overlapping region of a nucleus-nucleus collision,  $T_{AA}$ , the nucleon cross section,  $\sigma$ , and the Poisson distribution make-up the core of the Glauber model. For the total nucleus-meson scattering cross section, the equation has the following form:

$$\sigma_{tot}(VA) = \int d^2\vec{r} (1 - e^{-\sigma_{tot}(Vp)T_{AA}(\vec{r})}) \quad (2.20)$$

In Eq. 2.20, the term  $e^{\sigma_{tot}(Vp)T_{AA}}$  gives the probability of having no meson-nucleon scatterings from the Poisson distribution. The probability of having at least one scattering is given by subtracting one from the term  $e^{\sigma_{tot}(Vp)T_{AA}}$  in Eq. 2.20. As seen in Eq. 2.20, the Glauber model leverages scientific knowledge of the proton to understand of the nucleus. The Glauber model is the tool that combines the proton photoproduction data with nucleon distributions in the nucleus to produce a nuclear vector meson photoproduction cross section in the VMD approach.

Reversing the process used for the proton, Eq. 2.20, the meson nucleus scattering cross section, relates to forward nuclear photoproduction cross section through the optical theorem. The nuclear photoproduction cross section is the input to the calculation of the final result, the nuclear vector meson photoproduction cross section in UPC events. Eq. 2.21 uses the optical theorem to produce the nuclear photoproduction cross section from the nucleus-meson scattering cross section:

$$\sigma(\gamma A \rightarrow VA) = \frac{d\sigma(\gamma A \rightarrow VA)}{dt} \Big|_{t=0} \int_{t_{min}}^{\infty} dt |F(t)|^2 = \frac{\alpha \sigma_{tot}^2(VA)}{4\pi f_v^2} \quad (2.21)$$

$F$  in equation Eq. 2.21 is the Fourier transform of the nuclear density function,  $\rho_A$ . To produce the formula for calculating the UPC vector meson photoproduction cross section, Eq. 2.21 is combined with the photon flux incident on the nucleus, Eq. 2.17.

$$\sigma(AA \rightarrow AAV) = 2 \int dk \frac{dN_\gamma}{dk} \sigma(\gamma A \rightarrow VA) \quad (2.22)$$



The factor of 2 in Eq. 2.22 comes from the fact that both of the two colliding nuclei contribute. Combining the three elements of VMD, Eq. 2.22 is the final result of the VMD UPC photoproduction cross section calculation. Vector meson production rates in UPC collisions are predicted by Eq. 2.22, which can be confirmed or denied by experiment.

## 2.6 Leading Twist Approach Derivation

The LTA method for calculating UPC photoproduction cross sections combines elements of the Glauber model with direct use of gluon densities. The proton gluon density is modified by a nuclear modification function in the LTA method to produce the nuclear gluon density. The nuclear modification function converts the proton photoproduction cross section to a nuclear photoproduction cross section in the LTA method. The LTA method is different from the other methods in its direct use of the nuclear modification factor and how the nuclear modification factor calculation incorporates multiple scattering. The direct use of the nuclear modification factor produces the most gluon shadowing out of the three major methods, and results in the lowest cross sections. The LTA method is the easiest to constrain experimentally for this reason.

The LTA method uses the Weizsäcker-Williams approximation to calculate the photon flux created by the colliding nuclei. As in the VMD method, the probability of having no hadronic collisions modulates the flux. The photon flux for the LTA method has the following form [7]:

$$n_{\gamma/A}^i(\omega_\gamma) = \frac{2\alpha Z^2}{\pi} \int_{b_{min}}^{\infty} db \frac{x^2}{b} \left[ K_1^2(x) + \frac{K_0^2(x)}{\gamma_L^2} \right] P_0(b) P_C^i(b) \quad (2.23)$$

$$x = \frac{\omega b}{\gamma_L v}$$

The  $K_0^2(x)$  term contributes a photon flux in the transverse direction.  $P_C^i(b)$  is an additional modulation factor that requires various additional interactions. These interactions result in additional emissions of neutrons from the receding nuclei as the nuclei relax from excited states. The LTA flux reproduces the VMD result when the  $K_0$  term becomes negligible as  $\gamma_L$  approaches  $\infty$  and

$P_C^i = 1$  when all emissions are allowed. The terms  $P_C^i$  and  $K_0$  create additional ways to distinguish UPC events from nuclear collisions experimentally but leave the underlying interaction mechanism the same. For example, the additional terms in the LTA formulation of the photon flux produce calculations of asymmetric neutron emission, which separate UPC events from nuclear collisions.

The LTA method calculates the nucleon photoproduction cross section from the nucleon gluon density. Ref. [7] derives the nucleon cross section from derivations of the nucleon gluon densities from electron-proton scattering data and leading order perturbative quantum field theory calculations. The forward photoproduction cross section of the nucleon has the following form [7]:

$$\frac{d\sigma_{\gamma N \rightarrow J/\psi N}(t=0)}{dt} = \frac{16\Gamma_{l+l-}\pi^3}{3\alpha M_{J/\psi}^5} [\alpha_s \mu^2 x G_N(x, \mu^2)]^2 \quad (2.24)$$

Here  $G_N$  is the gluon density of the nucleon,  $x$  is the fraction of the nucleon's momentum the gluon carries, and  $\mu$  is related to momentum at which the nucleon is being probed, which is equal to  $M_{J/\psi}/2$  for  $J/\psi$  photoproduction. In Eq. 2.24 the nucleon cross section is explicitly connected to the gluon density. By connecting the gluon density to the cross section, Eq. 2.24 allows for the gluon density to be experimentally probed.

Ref. [7] exploits the optical theorem to relate the forward photoproduction cross section of the nucleon to the nuclear cross section. Eq. 2.25 gives the relation:

$$\sigma_{\gamma A \rightarrow J/\psi A}(\omega) = \frac{d\sigma_{\gamma N \rightarrow J/\psi N}}{dt}(\omega, t_{min}) R_g^2 \int_{t_{min}}^{\infty} dt |F(t)|^2 \quad (2.25)$$

$$R_g = \frac{G_A(x, \mu^2)}{A G_N(x, \mu^2)}$$

$R_g$ , the nuclear modification function, is the ratio between the gluon density of the nucleon,  $G_N$ , to the gluon density of the nucleus,  $G_A$ . As with the VMD method, the optical theorem relates the forward cross section,  $\frac{d\sigma_{\gamma N \rightarrow J/\psi N}}{dt}(\omega, t_{min})$ , to the total cross section,  $\sigma_{\gamma A \rightarrow J/\psi A}$ . The LTA method relates the measurable UPC photoproduction cross section to the gluon density of the nucleus. Eq. 2.25 further connects the gluon density of the nucleon to the relative reduction of the gluon

density in the nucleus through  $R_g$ .

From Eq. 2.25, the LTA method can predict the angular distribution of photoproduced  $J/\psi$  with respect to the beam axis. In Ref. [8] the angular distribution is expressed in the form of the rapidity dependency of the UPC photoproduction cross section.

$$\frac{d\sigma_{A_1 A_2 \rightarrow A_1 A_2 J/\psi}}{dy} = n_{\gamma/A_1}(y) \sigma_{\gamma A_2 \rightarrow J/\psi A_2}(y) + n_{\gamma/A_2}(-y) \sigma_{\gamma A_1 \rightarrow J/\psi A_1}(-y) \quad (2.26)$$

$$y = \ln\left(\frac{2\omega}{M_{J/\psi}}\right)$$

Eq. 2.26 is comprised of two terms, one for photons from the forward going nucleus interacting with the backward going nucleus, and a second for the reverse situation. The integration of Eq. 2.26 over  $y$  produces the factor of 2 that is present in Eq. 2.22. The rapidity distribution of the photoproduction cross section given in Eq. 2.26 provides a more detailed prediction and allows for more direct experimental comparison. Eq. 2.26 allows for comparison to rapidity regions that are covered by experiments.

The LTA method is distinct from the pQCD method and VMD method through the use  $R_g$ , the nuclear gluon modification factor. As opposed to using  $R_g$ , the pQCD method uses the nuclear gluon density, and VMD model uses proton photoproduction cross sections directly. In the LTA method,  $R_g$  is calculated through a combination of  $J/\psi$  photoproduction data from proton-electron scattering and DGLAP evolution equations, which incorporates nuclear multiple scattering effects [7]. The DGLAP evolution equations give the depends of nuclear gluon densities on the momentum scale at which the nucleus is probed,  $\mu$  in Eq. 2.24. The unique way the LTA method calculates  $R_g$  results in lower cross sections than the other major methods and allows for experimental sensitivity. Experimental measurements of the UPC  $J/\psi$  photoproduction cross section with CMS have the opportunity to distinguish whether  $R_g$  as calculated in the LTA method accurately predicts the gluon density of the nucleus.

## 2.7 Perturbative Quantum Chromo-dynamics

To calculate the UPC  $J/\psi$  photoproduction cross section, the pQCD method uses the nuclear gluon density to characterize the nucleus and the Weizsäcker-Williams approximation for the probing photon flux. The pQCD method combines these components such that the nuclear gluon density is a direct variable. The nuclear gluon density term in the pQCD formulation allows for the use of a variety of nuclear gluon density models. A range of nuclear gluon densities are present in the available models resulting in a wide range of cross section values. The UPC  $J/\psi$  photoproduction cross section is correlated with the gluon density of the nucleus rising with higher densities and shrinking with lower densities. In the pQCD approach, the calculation of the UPC  $J/\psi$  photoproduction cross section allows experiments to constrain many different nuclear gluon density models.

In the pQCD method, the photon interacts with the nucleus by fluctuating to a quark-antiquark pair. For  $J/\psi$ , the photon fluctuates to a  $c\bar{c}$  pair. The probability for the photon to fluctuate to a  $c\bar{c}$  pair depends on the  $M_{J/\psi}$ , the mass of  $J/\psi$ ,  $\Gamma_{l+l^-}$ , the  $J/\psi$  leptonic decay width, and  $\alpha$ , the electromagnetic coupling constant. These three variables connect the  $c$  quark to the electromagnetic force mediator, the photon. Recast as a  $c\bar{c}$  pair, the photon couples to the nuclear gluon density. Ref. [9] uses the fluctuation of the photon to a  $c\bar{c}$  pair as the foundation for calculating the forward  $J/\psi$  photoproduction cross section.

The  $c\bar{c}$  pair arising from the photon fluctuation scatters off the gluons of the nucleus. The density of gluons in the nucleus determines how likely and therefore how large the cross section is for the quarks to scatter and form a  $J/\psi$ . The forward scattering cross section is the portion of those scattering events which transfer the minimum amount of momentum between the photon and the nucleus. The forward cross section for  $J/\psi$  photoproduction in the nucleus has the following form [9]:

$$\left. \frac{d\sigma_{\gamma A \rightarrow J/\psi A}}{dt} \right|_{t=0} = \xi_{J/\psi} \left( \frac{16\pi^3 \alpha_s^2 \Gamma_{l+l^-}}{3\alpha M_{J/\psi}^5} \right) [xG_A(x, \mu^2)]^2 \quad (2.27)$$

In Eq. 2.27,  $\xi_{J/\psi}$  is an experimentally derived correction factor,  $\alpha_s$  is the strong coupling constant,

$x$  is the momentum fraction of the nucleus the scattering gluons carry, and  $G_A$  is the gluon density of the nucleus. Both the  $c$  and  $\bar{c}$  couple to the gluon density, and the double coupling results in the squared dependence of the cross section on the gluon density in Eq. 2.27. Fitting Eq. 2.27 to proton-electron scattering data sets  $\xi_{J/\psi}$  [9]. The forward scattering cross section given by Eq. 2.27 connects the photon flux to the gluon density and provides the input to calculate the total cross section by the optical theorem. Eq. 2.27 is the crux of how UPC measurements provide insight into the gluon content of the nucleus.

The optical theorem relates the forward cross section in Eq. 2.27 to the total photoproduction cross section. The total cross section calculated by use of the optical theorem gives the probability that a photon incident on the nucleus will produce a  $J/\psi$  regardless of the momentum transferred in the interaction. Ref. [9] gives the form of the total cross section equation:

$$\sigma_{\gamma A \rightarrow J/\psi A}(k) = \frac{d\sigma_{\gamma A \rightarrow J/\psi A}}{dt} \Big|_{t=0} \int_{t_{min}(k)}^{\infty} dt |F(t)|^2 \quad (2.28)$$

Here  $t_{min} = (M_{J/\psi}^2/4k\gamma_L)^2$ , which is the minimum amount of momentum transfer required to produce a  $J/\psi$  given the photon wave number  $k$ . The  $k$  dependence of  $t_{min}$  produces the rapidity,  $y$ , dependence of the total cross section. The total cross section for photoproduction, Eq. 2.28, provides the input to Eq. 2.26, which gives the rapidity dependence of the UPC photoproduction cross section. Eq. 2.28 as input to Eq. 2.26 allows for experimental comparison of the pQCD method to measurements of UPC photoproduction cross sections. With the pQCD method's direct use of the nuclear gluon density in Eq. 2.27, the pQCD method allows for experimental exploration of any gluon density model.

## 2.8 Incoherent Photoproduction

## 2.9 Photon Induced Nuclear Break-up

## 2.10 Theoretical Results

The UPC photoproduction cross section calculations depend significantly on how the nucleus is represented in the calculation. The results from the VMD, LTA, and pQCD methods vary from a relatively large cross section in the VMD model, ranging through a variety of values in the pQCD method, to a relatively small cross section in the LTA method. Each of these methods utilizes the same probe of the nucleus, the equivalent photon flux that is calculated using the Weizsäcker-Williams approximation. The three methods deviate in how they calculate the forward photoproduction scattering cross section. The differences in the UPC photoproduction cross sections predicted by the different models demonstrates the amount of experimental sensitivity there is to distinguishing between the models. The dependence of the cross section on rapidity shows where in phase space a measurement of the cross section is most sensitive.

The predicted value for the UPC  $J/\psi$  photoproduction cross section in PbPb collisions at the LHC differ widely depending on which of the three main methods is used. The cross section value calculated by Eq. 2.22 in the VMD, LTA, and the various gluon density models in pQCD method vary significantly. Table 2.1 gives the predicted values for the three main methods taken from Ref [10], Ref [7], and Ref [6]. The cross sections in Table 2.1 differ by a factor of  $\approx 4$  from the smallest to largest and create an experimental opportunity. The clear discrepancy between the models in Table 2.1 demonstrates the high amount of experimental sensitivity there is for distinguishing between the models.

The rapidity dependence of the cross sections determine which values of rapidity will be most sensitive to differences in the models. The rapidity dependence calculated by Eq. 2.26 overlap between the models at certain values of  $y$  leaving the models indistinguishable at that rapidity. Fig. 2.3 [11] shows the rapidity dependency of the UPC  $J/\psi$  photoproduction cross section for the

Model	$\sigma_{AA \rightarrow AAJ/\psi}(mb)$
VMD/STARlight MC	23
LTA	9
pQCD-MSTW08	34
pQCD-EPS08	7
pQCD-EPS09	14
pQCD-HKN07	23

Table 2.1:  $\sigma_{AA \rightarrow AAJ/\psi}(mb)$  the LTA, VMD, pQCD methods. Four different gluon density models are used in the pQCD method. STARlight is a simulation software package that utilizes the VMD model.

three main models including several different gluon density models using the pQCD method. In

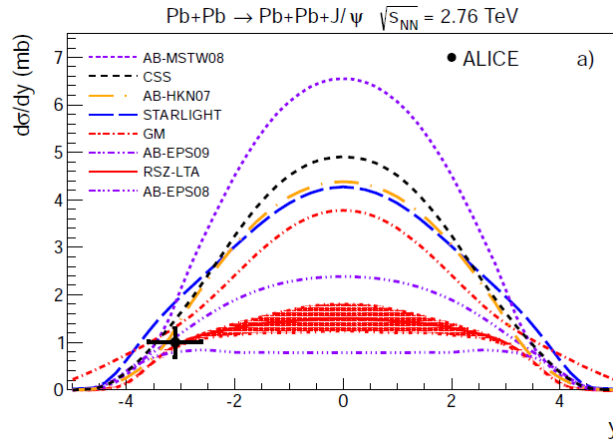


Figure 2.3: AB is the pQCD method, RSZ-LTA is the LTA method, and STARlight is the VMD model.

Fig. 2.3 at higher rapidities, in particular  $|y| > 3$ , the various models give similar values for  $d\sigma/dy$ . At  $y = 0$  the models vary the most. Fig. 2.3 shows that experiments that can measure  $J/\psi$  at  $y = 0$  have the best opportunity to distinguish between the models. The high sensitivity at  $y = 0$  creates an advantage for experiments that can measure particles with small rapidity and low momentum.

The UPC photoproduction models each have different shapes to their rapidity dependence. The slope of  $d\sigma/dy$  in Fig. 2.3 depends on the model. Through the rapidity region  $1 < |y| < 3$ , each of the models has a progressively steeper slope. The LTA method and the pQCD method utilizing the EPS08 gluon density model are relatively flat where as the VMD and other gluon

density models using the pQCD method have a noticeable slope. The differing slopes provide an additional experimental observable. The shape of the rapidity distributions provide experimental sensitivity at rapidities away from  $y = 0$  and creates an opportunity for experiments that can not measure  $J/\psi$  at  $y = 0$ .

The nuclear suppression factor,  $S$ , demonstrates the difference between how the models represent the nucleus.  $S$ , which is a ratio between the nuclear photoproduction cross section and the free nucleon photoproduction cross section, is a measure of how the nuclear gluon densities evolve in each of the models. Fig. 2.4 from Ref.[12] shows the nuclear suppression, which is equivalent to  $R_g$  in Eq. 2.25, for the LTA and pQCD method. Fig. 2.5 shows the nuclear suppression for

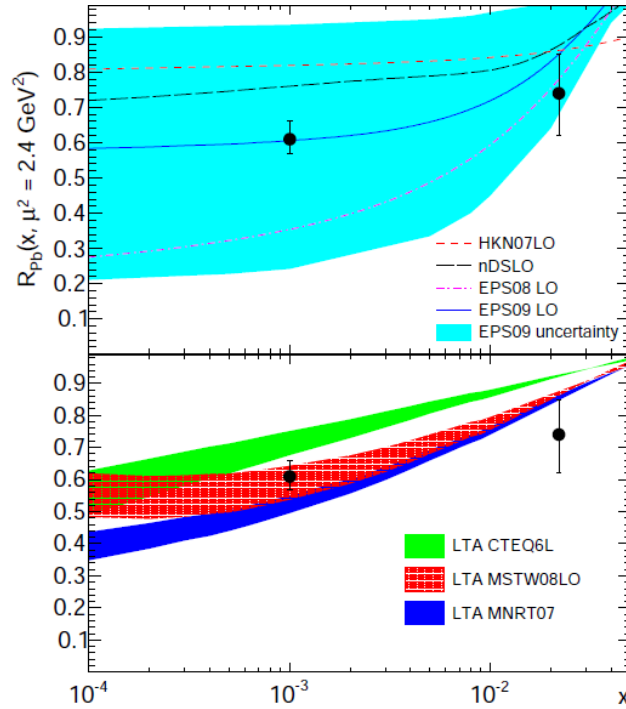


Figure 2.4: Nuclear suppression factor,  $S$ , in the pQCD and LTA methods.

the VMD method [12]. Fig. 2.5 and Fig. 2.4 show that as the momentum of the probing photon goes up, increasing  $W_{\gamma p}$ , and momentum of the probed gluon goes down, decreasing  $x$ , the nuclear gluon density decreases relative to the free nucleon. The nuclear suppression factor,  $S$ , allows for the different models' representations of the gluon content of the nucleus to be directly compared to each other and to data.  $S$  can be measured from data by assuming a Weizsäcker-Williams photon



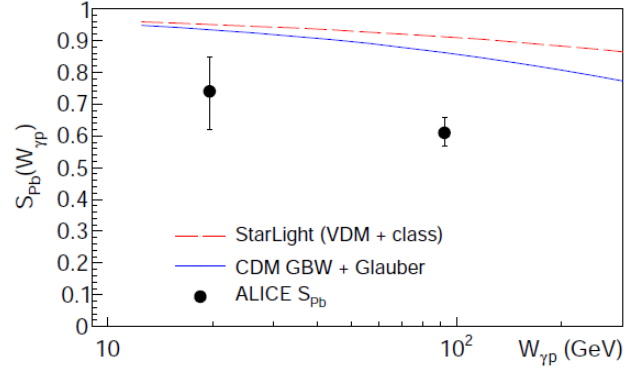


Figure 2.5: Nuclear suppression factor,  $S$ , in VMD method.

flux and provides insight into nuclear gluon densities.

# Chapter 3

## The CMS Detector

CMS is housed at interaction point 5 of the LHC. The LHC is designed to pursue physics at the TeV scale. This is the scale where electroweak symmetry breaking is believed to occur [?]. While this means that the search for the standard model Higgs is the central driving design consideration, the wide range of possibilities for finding new physics signals requires a general purpose detector. The expedient discovery of new physics through low cross section interactions requires high luminosity. This consideration leads inevitably to pile up, where multiple collisions occur at a single bunch crossing. At peak luminosity the LHC is expected to produce on average 20 hard proton-proton (pp) collisions per bunch crossing [1]. These particle physics considerations of high multiplicity due to pileup and the need for a general purpose detector make CMS serendipitously well suited for heavy ion physics.

The general purpose design of CMS is dominated by the massive 4T superconducting solenoid at its core. The magnet is 13m long with a 6m diameter, and pushes the limits of power and compactness [1]. These two conflicting limits are achieved through the novel design of interweaving structural and conducting elements together in the coil of the solenoid.

Within the solenoid reside three different sub detectors. The inner most is the world's largest silicon tracker [1]. The tracker is surrounded by a highly effective lead tungstate crystal electromagnetic calorimeter (ECAL). ECAL is encapsulated in a brass scintillating hadronic calorimeter

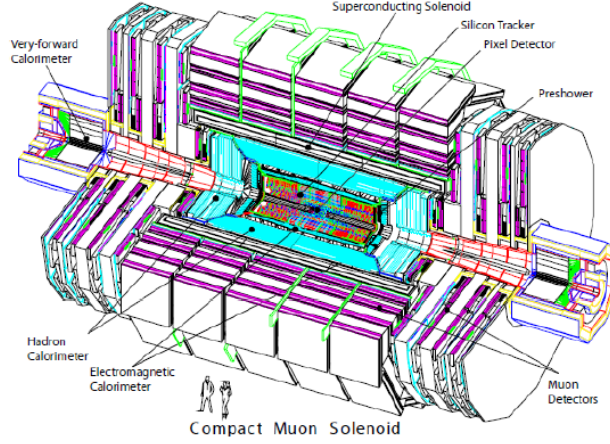


Figure 3.1: The Compact Muon Solenoid from Reference [1].

(HCAL). Outside the magnet, muon chambers are used to aid in the measurement and triggering of muon events. Altogether CMS weighs 12,500 metric tons, has a diameter of 14.6m, and a length of 21.6m [1].

The Silicon Tracker is the innermost sub-detector of CMS, and has active elements as close as 4.4cm to the interaction point [1]. The tracker has a length 5.8m, a diameter of 2.6m and covers a range in pseudorapidity of  $|\eta| < 2.5$ . Pseudorapidity is defined as  $\eta \equiv -\ln(\tan(\theta/2))$ , where  $\theta$  is the polar angle, and  $\phi$  is the azimuthal angle with respect to the beam axis. At the center of the tracker are three rings of silicon pixels around the beam with two disks of silicon pixels to cap the rings. The pixel portion of the silicon tracker is comprised of  $66 \times 10^6$  pixels. The silicon pixels are surrounded by silicon strips. The silicon strips are separated into 4 different sections: the Tracker Inner Barrel, the Tracker Inner Disk, the Tracker Outer Barrel, and the Tracker End Caps. The silicon strip detectors as a whole are comprised of  $9.3 \times 10^6$  silicon strips. The high number of pixels and strips allow for the ability to distinguish and collect enough distinct points to reconstruct the path of the 1000 or so charge particles per bunch crossing expected at peak luminosity [1].

The next detector beyond the tracker is ECAL. ECAL is made of 61,200 lead tungstate ( $\text{PbWO}_4$ ) crystals in the central barrel and 7,324 on each of the two endcaps [1]. The barrel (EB) covers a pseudorapidity range  $|\eta| < 1.479$  and has an approximate  $\eta - \phi$  segmentation of  $0.0174 \times 0.0174$ . Lead tungstate is very dense, which is reflect in the high number of interaction lengths the short

depth of one crystal provides. The crystals of the barrel have a depth of 230 mm corresponding to 25.8 radiation lengths ( $X_0$ ). The radiation length is the mean distance a high energy particle travels before giving up one e-fold of kinetic energy through electromagnetic interactions. For example, after one radiation length  $E \rightarrow E/e$ , where  $e = 2.71828183$ . The endcaps (EE) cover the pseudorapidity region  $1.479 < |\eta| < 3$ . In the endcap the crystals have an exposed area of  $28.62 \times 28.62$  mm<sup>2</sup>, and a depth of 220 mm corresponding to 24.7  $X_0$ . The energy resolution of the ECAL as measured by test beam data can be seen in Figure 3.2.

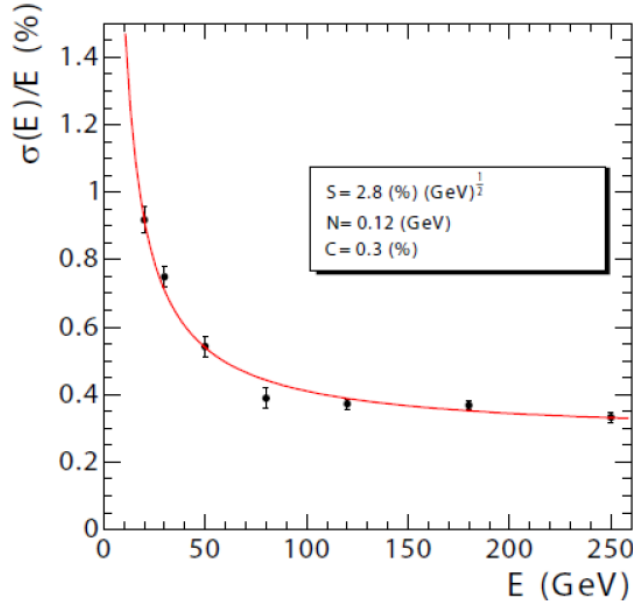


Figure 3.2: The energy resolution of ECAL as a function of energy from Reference [1].

The HCAL like the ECAL has both a barrel (HB) and endcaps (HE). The pseudorapidity region  $|\eta| < 1.3$  is covered by HB [1]. HB has an  $\eta - \phi$  segmentation of  $0.0897 \times 0.0897$ , and is 25 times more sparsely granulated than EB. HE covers the pseudorapidity region  $1.3 < |\eta| < 3$ . HE, like EE and the tracker endcaps, is aligned perpendicular to the beam axis resulting in granularity that changes with  $\eta$ . In the region  $1.3 < |\eta| < 1.6$  HE has an  $\eta - \phi$  segmentation of  $0.0897 \times 0.0897$ . The  $\eta - \phi$  segmentation roughly doubles to  $0.17 \times 0.17$  in the region  $1.6 < |\eta| < 3$ . The energy resolution of the barrel and endcaps can be seen in Figure 3.3. The thickness of the hadronic calorimeter is best described in interaction lengths, the mean distance for a particle to give up an e-fold of energy through nuclear interactions. At  $\eta = 0$  the barrel has a thickness 5.82 interaction

lengths ( $\lambda_I$ ), and increases as the path length through the material increases to  $10.6 \lambda_I$  at  $|\eta| = 1.3$ .

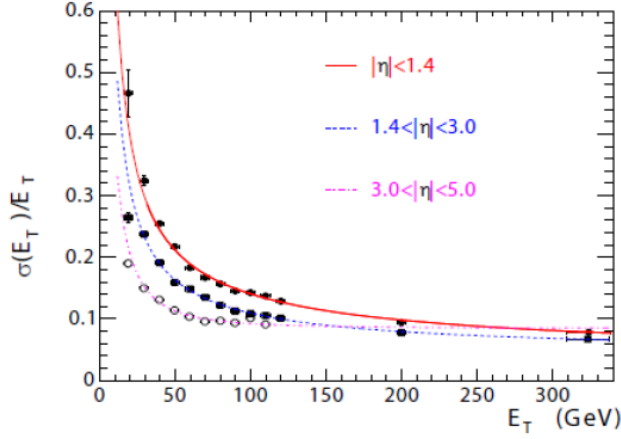


Figure 3.3: The  $E_T$  resolution of HCAL as a function of  $|\eta|$  and  $E_T$  from Reference [1].

In addition to HB and HE, HCAL has two additional calorimeters. Because the space between ECAL and the magnet is restricted to 1.18 m, an outer hadronic calorimeter section (HO) is placed beyond the magnet in the region  $|\eta| < 1.3$  [1]. The main function of HO is to collect energy from the highest energy hadrons before they reach the muon system. HO is not used in this analysis, but does contribute to the material budget. To increase the total calorimetric coverage, HCAL also has a quartz fiber calorimeter (HF) in the forward region,  $3 < |\eta| < 5$ . For the majority of HF's 13  $\eta$  rings the  $\eta - \phi$  segmentation is  $0.175 \times 0.175$ . In the lowest  $|\eta|$  ring the segmentation is  $0.111 \times 0.175$  in  $\eta - \phi$ . In the highest two  $|\eta|$  rings the segmentation in  $\phi$  is 0.349, with an  $\eta$  segmentation of 0.175 in the outer and 0.300 in the innermost ring. The longitudinal direction is effectively segmented by using short fibers and long fibers. The measure energy deposited deeper than 22 cm is measured in both the short and long fibers, where as the long fibers are present throughout. This allows electromagnetic showers to be distinguished from purely hadronic showers [1]. The energy resolution for HF can be seen in Figure 3.3.

Beyond HF there are two more detectors in the forward region. CASTOR covers the range  $5.2 < \eta < 6.6$  on the positive side of the beam. The Zero Degree Calorimeters (ZDC) sit between the beam pipes on either side of the interaction point covering the area around  $\theta = 0$ ,  $|\eta| > 8.3$ . Both

detectors are tungsten quartz Cerenkov detectors, and can contribute to the proposed measurement. In heavy ion collisions the ZDC has the ability to measure neutral particles that do not participate in the collision [1]. CASTOR extends the total coverage of the CMS as whole giving more access to low-x physics [1].

The muon system resides just outside of the superconducting magnet. It consists of three complementary systems: drift tube (DT) chambers in the barrel, cathode strip chambers (CSC) in the endcaps, and resistive plate chambers (RPC) in both the barrel and endcap regions [1]. Ultimately the muon system is most useful for triggering on muons [1].

The heavy ion community is making use of the capabilities of CMS in a myriad of ways. The muon trigger has been used in the search for suppression of quarkonium states. This is an important probe of the correlation length within the hot dense state known as the quark gluon plasma (QGP). The tracker has been utilized for to study charged particle multiplicities, and and elliptical flow, two probes of the thermal expansion of the QGP. HCAL has aided in measuring jet suppression, which probes the strength with which the QGP interacts with strong interacting objects. Through its general purpose design and its ability to handle the high multiplicities produce by the LHC, CMS proves to be an excellent detector for investigating strongly interacting mater through heavy ion collisions.

## **3.1 Trigger**

The CMS trigger is two teired. The L1 trigger is the lower level hardward based system. The High Level Trigger (HLT) is software base and runs on a computer farm at point 5 where CMS is housed.

# Chapter 4

## Analysis

### 4.1 MC Simulation

Monte Carlo (MC) simulations are used to understand how the detector effects the measurement. Two main classes of Monte Carlo (MC) simulation samples were used. The first class uses STARlight to generate events. The Second class uses PYTHIA6 to create and decay  $J/\psi$ s with a given input  $p_T$  and rapidity distribution.

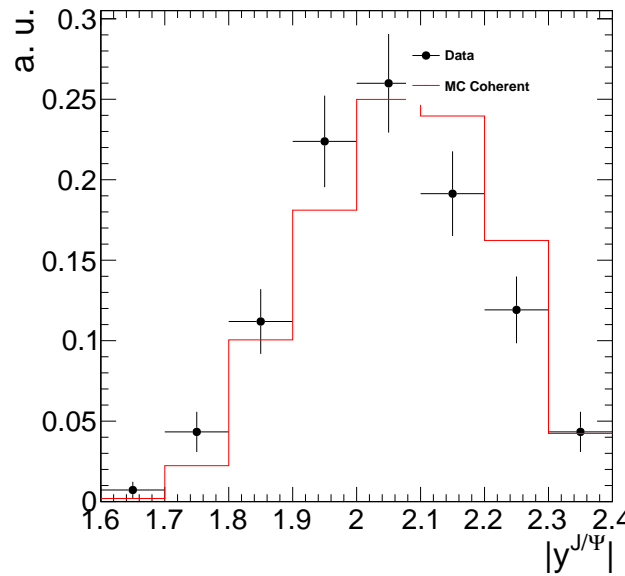


Figure 4.1: Comparison of the of the dimuon rapidity distributions between coherent MC sample and Data.

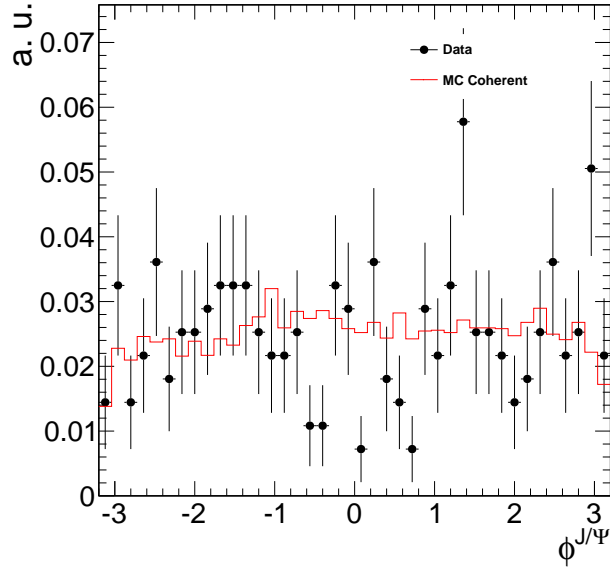


Figure 4.2: Comparison of the of the dimuon  $\phi$  distributions between coherent MC sample and Data.

## 4.2 Trigger Development

Prior to the 2011 LHC PbPb run, UPC events had not been directly studied in PbPb collisions using CMS. Design of the UPC triggers required studies of the 2010 data to estimate rates and assure that the bandwidth used by these trigger would be sufficiently low. All the different physics analyses must share the limited readout rate of the detector. For this reason, conservation of bandwidth was a major design consideration.

To estimate the 2011 rates prior to the run, the 2010 rates were used to extrapolate to the interaction rate of the 2011 run. The unique UPC triggers were estimated by combining existing triggers from the 2010 run. By calculating the ratio between the UPC trigger rates and the minimum bias trigger rate, the UPC trigger rates were scaled up to the 2011 interaction rates using the 2010 data. The extrapolated rates allowed for a package triggers to be created, which fit within the bandwidth requirement of CMS Heavy Ions.

The trigger package for 2011 contained ZDC based efficiency monitoring triggers, muon and electron based triggers for measuring  $J/\psi$ , and backup triggers in case there was a problem with



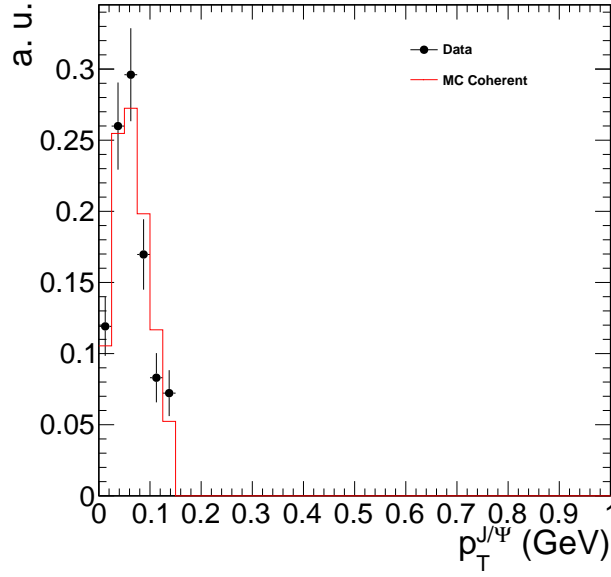


Figure 4.3: Comparison of the of the dimuon  $p_T$  distributions between coherent MC sample and Data.

the original muon and electron triggers. In order to recorded the trigger efficiency monitoring data, the ZDC triggers had to be prescaled to a lower rate. The scaling down of the monitoring triggers were setup to assure overlap with the signal triggers. By balancing the competing objectives of rate reduction and increasing the overlap between the monitoring and signal triggers, the prescales for the trigger were as seen in Table .

#### 4.2.1 L1 Trigger

The goal of the L1 triggers was to record enough data to measure dimuons and dielectrons in UPC events. To achieve this, the loosest muon trigger and lowest threshold ECAL triggers where paired with a trigger on energy in the ZDC and a veto on energy in the BSC or HF. The L1 package that was constructed for the analysis of UPC  $J/\psi$  is presented in Table 4.1.

The cumulative L1 trigger rate for all the UPC L1 trigger seeds was required to be 200 Hz. This requirement stemmed from the need to keep the tracker read-out rate low. The trackers baseline voltage can fluctuate due to the high tracker hit multiplicities in PbPb collisions. In order to monitor the zero suppression of the tracker, the zero suppression algorithm was executed using the HLT

L1 Trigger Seed	Type
L1_MuOpen_ZdcCalo_NotBscMinBiasThresh2_BptxAND	Physics
L1_EG2_ZdcCalo_NotBscMinBiasThresh2_BptxAND	Physics
L1_EG5_ZdcCalo_NotBscMinBiasThresh2_BptxAND	Physics
L1_ZdcCaloMinus_BptxAND	Monitor
L1_ZdcCaloMinus_BptxAND	Monitor
L1_MuOpen_ZdcCalo_NotHcalHfCoincidencePm_BptxAND	Backup
L1_EG2_ZdcCalo_NotHcalHfCoincidencePm_BptxAND	Backup
L1_EG5_ZdcCalo_NotHcalHfCoincidencePm_BptxAND	Backup

Table 4.1: List of 2011 L1 seeds.

computing farm rather than the in the tracker firmware. The additional computing cycles needed to run the zero suppression set the limit for L1 bandwidth.

#### 4.2.2 HLT Trigger

As opposed to the L1 trigger, which reads out the tracker, the HLT has access to the tracker information. Reconstruction of a track in the pixel detector is used by the UPC paths. The use of the pixel detector only, as opposed to using the whole tracker including the silicon strip detector, allows for quick track reconstruction saving computing cycles. The requirement of at least one reconstructed pixel track for the HLT triggers was designed to reject backgrounds where no particles are reconstructed by the tracker.

HLT Trigger	
HLT_HIUPCNeuMuPixel_SingleTrack	Physics
HLT_HIUPCNeuEG2Pixel_SingleTrack	Physics
HLT_HIUPCNeuEG5Pixel_SingleTrack	Physics
HLT_HIMinBiasZDC_Calo_PlusOrMinus_v1	Monitor
HLT_HIMinBiasZDC_PlusOrMinusPixel_SingleTrack_v1	Monitor
HLT_HIUPCNeuHcalHfMuPixel_SingleTrack	Backup
HLT_HIUPCNeuHcalHfEG2Pixel_SingleTrack	Backup
HLT_HIUPCNeuHcalHfEG5Pixel_SingleTrack	Backup

Table 4.2: List of 2011 HLT trigger.

The total HLT output for the UPC trigger paths was 20 Hz. The limiting factor for the HLT rate was the amount of disk space available to store the data.

## 4.3 Data Sets and Event Selection

### 4.3.1 Data Set

In order to investigate novel physics processes like UPC  $J/\psi$  production, the LHC has delivered unprecedented amounts of data. The data for this analysis was recorded during the 2011 LHC PbPb run. During this period,  $157 \mu b^{-1}$  were recorded by the CMS detector, corresponding to over a billion PbPb collisions. Of this,  $143 \mu b^{-1}$  are used in this analysis.

Three specially selected samples are used (see Table 4.3). These samples were recorded using subsets of the triggers found in Section 4.2. The  $J/\psi$  events discussed in this thesis were obtained analyzing the sample labeled in Table 4.3 as physics. A minimum bias sample was recorded for the sake of estimating efficiencies. Last, a zero bias sample was recorded for investigating the ZDC and the noise distributions of HF. By recording this hierarchy of samples, interesting events are selected with a much higher purity in the physics sample, while the zero bias and minimum bias samples allow for the investigation of the selection criteria.

To record the physics sample containing the  $J/\psi$  signal, a muon trigger was paired with a veto on energy in the BSC and a requirement that there be energy in at least one of two sides of the ZDC. This trigger utilizes the unlikely chance of having overlapping noise in the ZDC and muon detector. Because of the characteristically low momentum of UPC  $J/\psi$  as compared to  $J/\psi$  created by other physics process, the loosest muon trigger was used. The trigger rejects muon noise by requiring that an interaction took place that deposits energy in the ZDC. Contributions from hadronic interactions are reduced by the veto on the BSC. In this way the balance between reducing the rate and maximizing the efficiency was struck, allowing for the data to be recorded without producing high rates resulting in dead time for the detector.

In order to investigate the muon trigger and the other parts of the events selection, a minimum bias sample was recorded using the ZDC. For ZDC triggered sample, any event which had energy consistent with at least one neutron in either of the two sides of the ZDC was recorded. This process is much more common than the UPC  $J/\psi$  production. For this reason, the rates of this trigger are

Sample	Events	$L_{int}$
Physics	300K	143.3 $\mu b$
Minimum Bias	100K	X
Zero Bias	5M	580 b

Table 4.3: Integrated luminosities and number of events for the three samples used in this analysis.

much higher than the physics trigger, and only a small sub set of these events are recorded. From this trigger the pixel track efficiency was estimated.

In addition to the minimum bias and physics sample, a zero bias sample was recorded to examine the ZDC trigger and the HF noise distributions. The zero bias trigger fired every time both beams passed through CMS. Only 4 events out of every million triggered were recorded for this sample. This sample allowed for an unbiased measurement of the ZDC trigger efficiency as discussed in Section 4.6. Because the zero bias trigger does not require any activity in any of the CMS sub detectors, the sample contains very few hadronic collisions. This allowed for a measurement of the electronic noise distributions in the HF, which will be discussed in the next section.

The integrated luminosity for each of the three samples is calculated by recording activity in HF. The cross section for HF activity is measured from a van der Meer scan, and the cross section was found to be X. In this way the amount of integrated luminosity for any period running is related to the activity in HF. An additional method was used to cross check the integrated luminosity obtained by the van der Meer scan technique. The integrated luminosity can also be measured by counting the events that fire the L1 minimum bias trigger together with the inelastic PbPb cross section.

### 4.3.2 Event selection

The analysis described in this thesis focuses on UPC  $J/\psi$ s decaying to muons. The trigger used for this analysis recored X events. A set of off-line cuts were applied to increase the relative contribution of UPC events relative to background processes. The following cuts were applied.

Two sets of event selection cuts are applied to reject background events. The first set rejects

background from the beam. The second reject events where hadronic collisions have occurred.

To reject beam induced background the following cuts were applied:

- The reconstructed vertex must be within  $X$  cm in the transverse direction and  $X$  cm in the longitudinal direction. This cut assures that reconstructed particles come from interactions between the two beams rather than event where one of the two beams interact with gas particles near the interaction point.
- Beam halo muons were rejected using the timing of the muon hits. The beam halo cut rejects events where muons surrounding the beam stream through the detector.
- Pixel cluster shape should be compatible with the vertex. This cut requires that energy deposits in the silicon tracker point back to the reconstructed primary vertex.

These beam background cuts do not reject any UPC  $J/\psi$  candidates.

The second set of background rejection cuts were designed to reduce contamination from hadronic interactions.

- No more than 2 reconstructed tracks in the event. The track requirement rejects events that produce many charged particles.
- Maximum reconstructed hit energy in HF was required to be below the threshold for electronic noise. Nearly all hadronic interactions ( $\sim 98\%$ ) produce particles in the range  $3 < |\eta| < 5$  covered by the HF detector. By requiring that the energy deposits in HF resemble noise, nearly all elastic hadronic collisions are expected to be rejected.
- Energy in the ZDCs consistent with neutrons on only one side of the interaction point In hadronic interactions both nuclei break-up. By requiring that ZDC only reconstruct neutrons on one side of the interaction point, hadronic interactions that produce neutrons on both sides were rejected.

Each of these cuts are designed to reject topologies produced by hadronic interactions. The effect of these cuts can be seen in Table  $X$ .

The following standard muon quality cuts are applied:

- Tracker track matched with at least one muon segment (in any station) in both X and Y coordinates ( $< 3 \sigma$ ).
- Cut on number of tracker layers with hits  $> 5$ .
- Number of pixel layers  $> 0$ .
- The  $\chi^2$  per degrees of freedom of the track fit  $< 3$ .
- Loose transverse and longitudinal impact parameter cuts, with in 3 cm in the transverse direction and withing 30 cm in the longitudinal direction with respect to the primary vertex.

These cuts are applied to reduce the number of fake muons.

## 4.4 Break up determination

### 4.4.1 ZDC Signal Reconstruction

There are 18 zdc channel. There are 4 hadronic channels and 8 electromagnetic channels on each side of the CMS. To measure neutrons in the ZDC the charge in each channel is first converted to a signal.

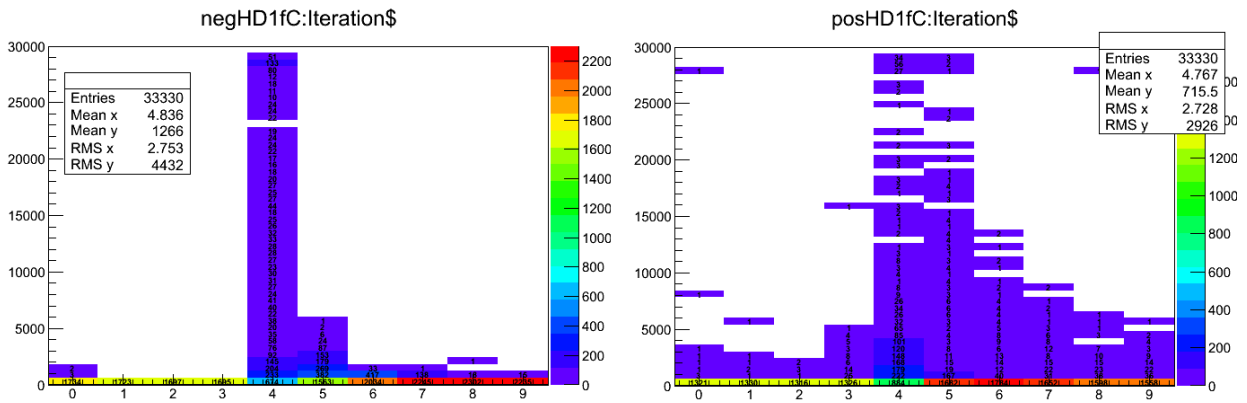


Figure 4.4: ZDC pluse shape.

Channel Signal definition: The signal in the zdc calculated two ways.

1. Method 1

(a) signal: 4,5,6

(b) background: 1,2

2. Method 2

(a) signal: 4

(b) background: 5

As seen in Fig 4.4, method 1 uses all the dominant signal time slices and uses the maximum number of “clean” non signal time slices to estimate the noise pedestal event by event. This minimizes the effect of random noise time slice by time slice by averaging over the maximum number of time slices per event.

Method 2 uses only the two time slice that are most likely to be above zero. Because all signal that is less than zero is not measured, method 1 only allows for a noise pedestal measurement half the time.

From these two methods the ZDC+ and ZDC- energy spectra near the one neutron peak are plotted in Fig. 4.5. While method 1 in blue and method 2 in red not differ much in ZDC-, the clear separation of the one neutron peak signal from the noise peak about zero is evident.

#### **4.4.2 Determination of the one neutron thresholds**

The ZDC thresholds used to establish the break-up mode were measured from zero bias data. By using this dataset, the spectrum does not contain a trigger bias. The trigger requirement in the event is that both beams were present in CMS. This does however include a significant electronic noise contribution due to events where no neutrons are emitted in the direction of the zdc. To separate the signal from the electronic noise additional cuts are applied in the zero bias data.

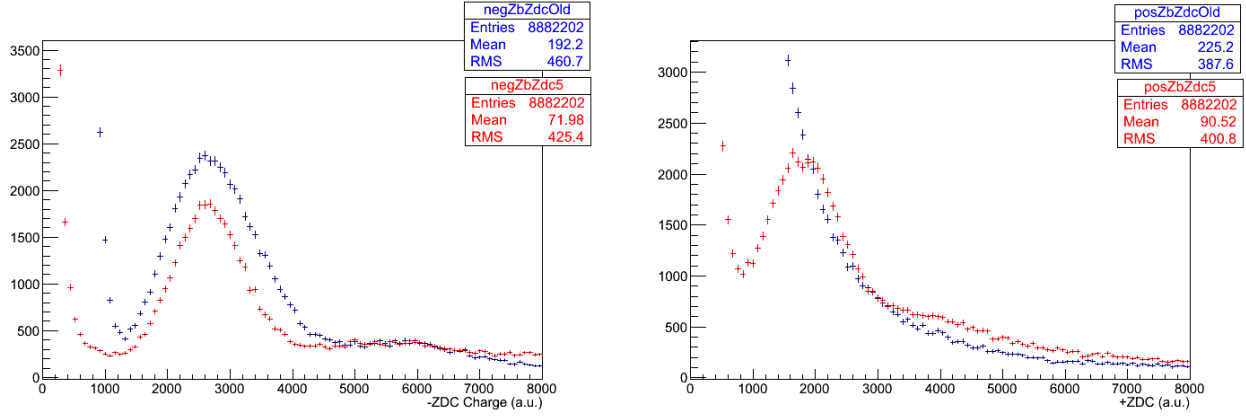


Figure 4.5: Comparison of ZDC signal reconstruction methods.

In Fig. 4.4 the pulse shape peaks in the peaks in the fourth time slice, for electronic noise however, any of the ten time slices are equally likely to have a peak value. Using this fact, signal can be preferably selected by requiring that the hadronic channels of the ZDC have a peak signal in the fourth time slice. In Fig. 4.6 no noise subtraction is used. As each additional hadronic channel

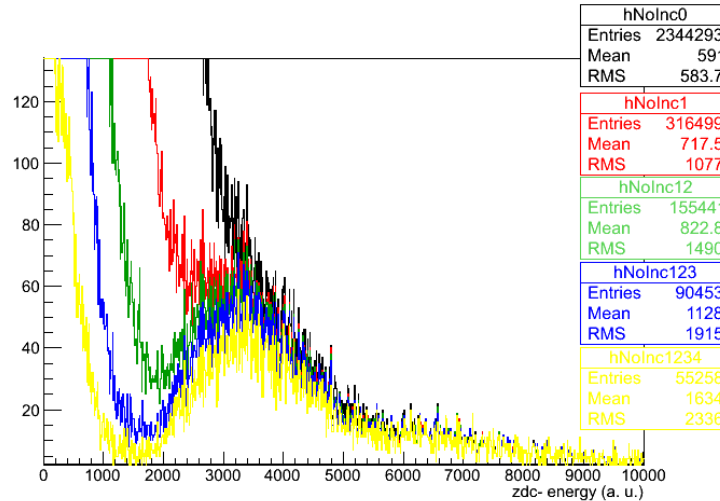


Figure 4.6: Effects of requiring in time signal in ZDC hadronic channels.

is required to have a maximum signal in the fourth time slice, the single neutron peak emerges. Using the noise subtraction method described by Method 1, the same signal emerges. Fig. 4.7 confirms that both noise subtraction and the timing require produce the same signal. This gives confidence that the signal is not an artifact of either cut, but the true neutron signal.

Fig. 4.7 and Fig. 4.5 demonstrate the consistence of the using timing cuts and noise subtraction



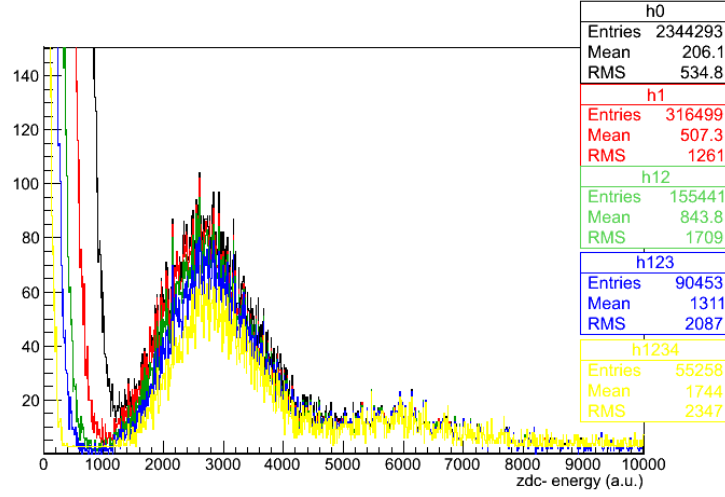


Figure 4.7: Effect of ZDC signal timing requirements after noise subtraction.

to enhance the signal neutron peak. Fig. 4.7 confirms the legitimacy of the noise subtraction method in  $ZDC^-$  by showing that the same signal emerges from the noise subtraction method as the timing method. Fig. 4.5 demonstrates the correspondence between noise subtraction method 1 and method 2 on in  $ZDC^-$  where signal is better separated from the electronic noise. This allows for confidence that the signal seen in  $ZDC^+$  using method 2 is the one neutron peak.

The spectrum for method 1 and 2 are fit to a series of Gaussians. The electronic noise is fit to a

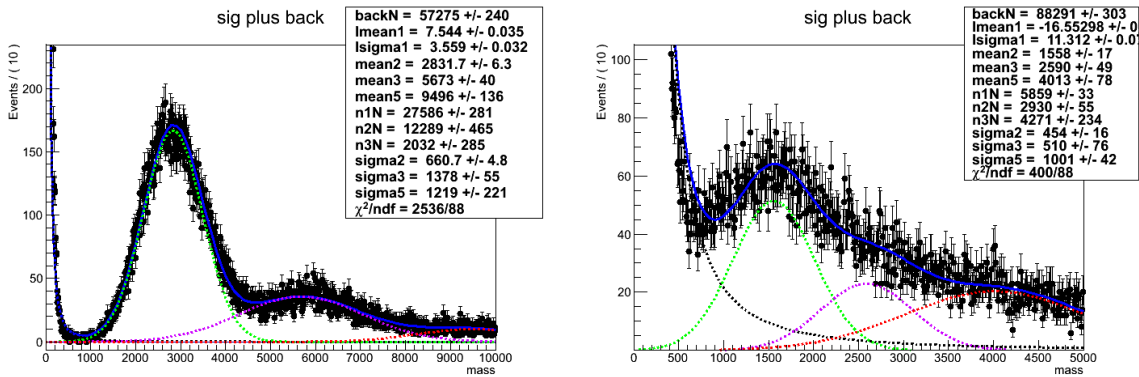


Figure 4.8: Fit to charge spectrum from  $ZDC^-$  (left) and  $ZDC^+$  (right) using method 1

Gaussian about zero. The one, two, and three neutron peaks are fit Gaussians that are successively broader. The mean of each peak was initially set to multiples of the mean of the one neutron peak. The threshold for a neutron in the ZDC was taken from the fits in Fig. 4.8 and Fig. 4.9. Any signal

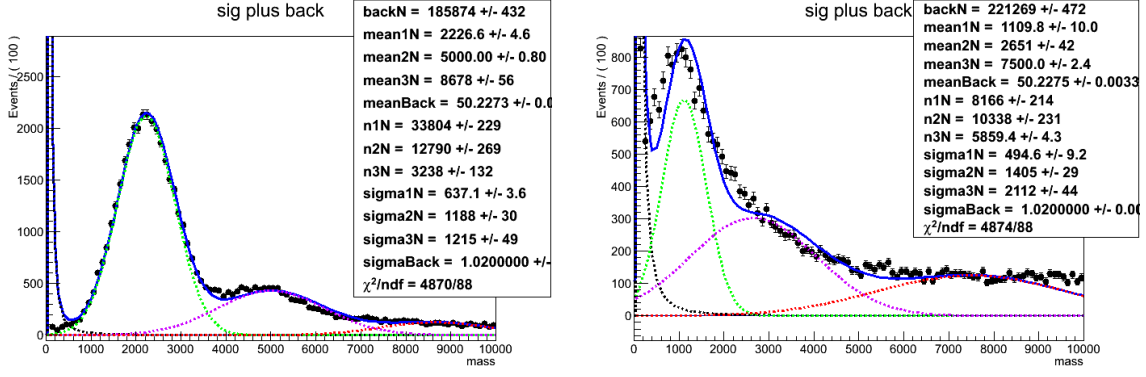


Figure 4.9: Fit to charge spectrum from ZDC<sup>-</sup> (left) and ZDC<sup>+</sup> (right) using method 2

greater  $2\sigma$  below the mean of the one neutron peak was considered signal.

## 4.5 Signal extraction

The invariant mass distribution for opposite sign dimuons is shown in Figure 4.10. A  $J/\psi$  signal is clearly visible together with tails at higher and lower mass due to the photon-photon process. A fit to the invariant mass distribution was done using a Gaussian and a Crystal Ball function to account for the  $J/\psi$  signal and a first and second order polynomial function for the photon-photon process. The extracted number of  $J/\psi$  candidates from this fit includes all  $J/\psi$ s in the mass window that pass the analysis cuts.

The  $p_T$  spectrum is fit using templates from the three physics MC samples. These contributions display a different shape in transverse momenta. For this reason, the number of coherent  $J/\psi$  candidates were extracted from the dimuon  $P_t$  distribution, around the  $J/\psi$  mass, after fitting together MC templates for both signal and background.

Fig. 4.10 demonstrates the small dependence the raw  $J/\psi$  yield has on the fitting function. Both fit functions agree well, with reduced  $\chi^2$  values below one. The Crystal ball fit give an upper estimate for the  $J/\psi$  yield. The Gaussian fit gives a lower estimate. The main difference comes from the lower mass tails. In the Crystal ball fit the lower tail is considered to be signal due to shifting of the mass spectrum to lower mass due to radiation from the final state muons. In the

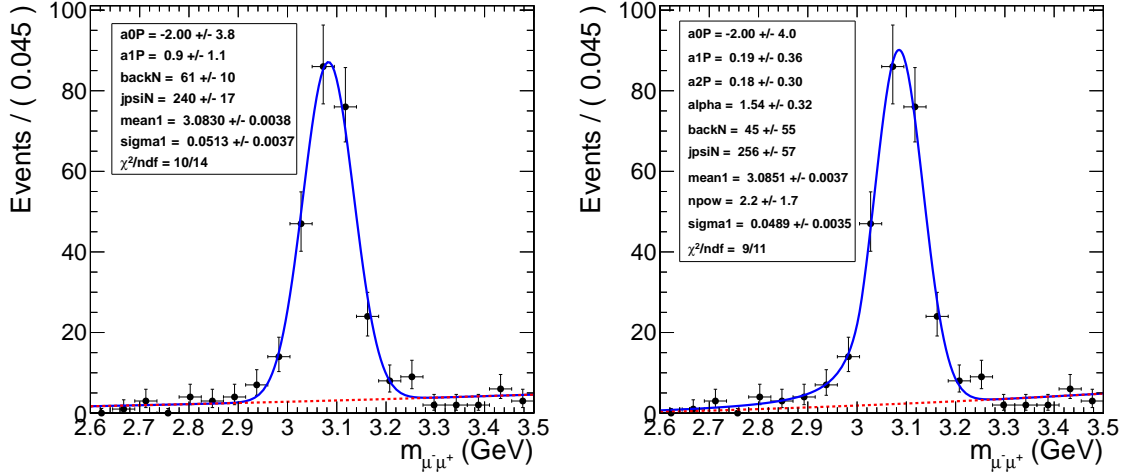


Figure 4.10: Mass fit to  $J/\psi$  using Gaussian (Left) and Crystal Ball (Right) for the signal and a polynomial for the background

Gaussian fit the lower mass tail is considered to be background and the signal is sharper.

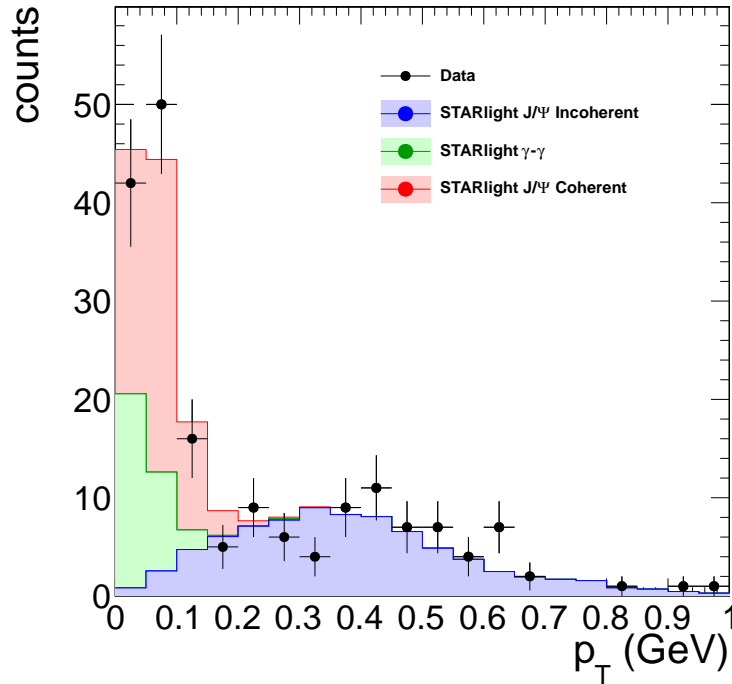


Figure 4.11: Coherent, incoherent, and photon-photon process  $p_T$  template fit to data.

The templates for the fit come from the three STARlight M.C. samples. The normalization for the coherent and incoherent templates are left free. The shape of the photon-photon process and coherent  $J/\psi$  are very similar in  $p_T$ . These two shapes normalizations are highly anti-correlated

in the fit. To address this issue the template from the photon-photon process was fixed to the cross section value given by STARlight and normalized to the integrated luminosity of the data. The normalization for the photon-photon template was allowed a range of 20% due to the 20% uncertainty in the STARlight cross section.

## 4.6 Efficiency determination

### 4.6.1 Muon Efficiencies

The muon efficiencies are measured from M.C and data. The M.C. based measurement accounts for the detector acceptance and the efficiency of the muon quality discussed in Section 4.3. The trigger efficiencies were measured by tag and probe.

To measure the detector acceptance, the muon daughter reconstruction efficiency is measured.  $\epsilon_{reco}^{\mu} = \frac{N_{reco}^{\mu}}{N_{gen}^{\mu}}$  Muon daughter detectability cuts were established from Fig. 4.12. All muons that were reconstructed with an efficiency better than 20% were declared detectable. Fig. 4.12 shows that reconstruction of the muon daughters does not depend on the generator used. The ability to reconstruct a muon depends only on the detector.

CMS has a limited acceptance for  $J/\psi$ s. This is particularly the case for  $J/\psi$ s with low momentum like those produced in UPC events. To measure the CMSs acceptance for  $J/\psi$ , reconstructed dimuon candidates were considered detectable if both reconstructed daughters in fell into the 20% detectability region defined by Fig. 4.12. The acceptance of the reconstructed dimuons are calculated from MC in using the following formula:

$$A = \frac{N_{detectable}(y, p_T)}{N_{gen}(y, p_T)} \quad (4.1)$$

From Eq. 4.1, the acceptance for  $J/\psi$  was calculated as a function of  $y$ , and  $p_T$  (see Fig. 4.13).

Tag and probe method is used to measure the trigger efficiency of the muon daughters. The method uses a tag and probe pairs where the high quality tag is paired with a lower quality probe.

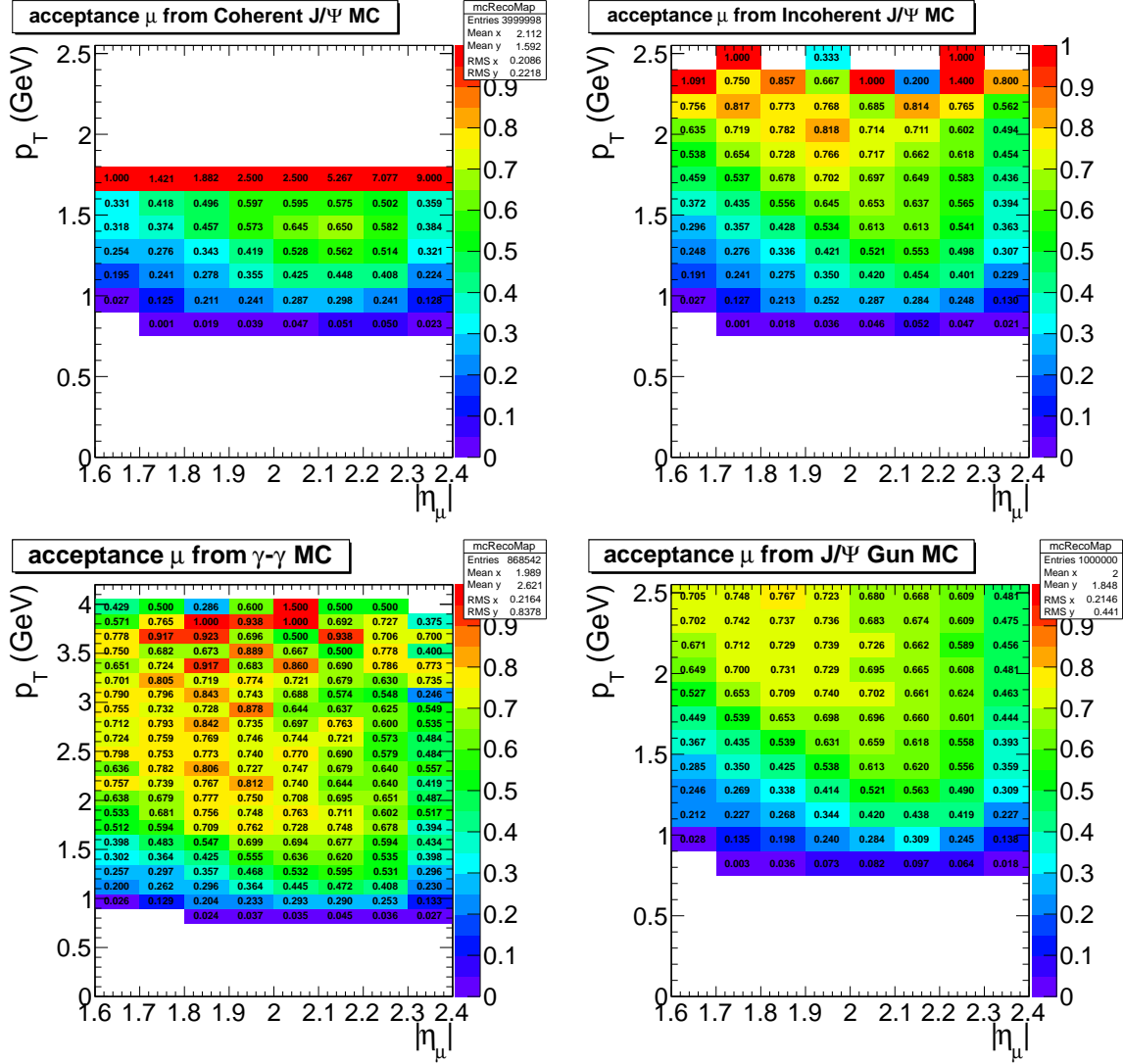


Figure 4.12: Muon daughter detectability from coherent J/ψ, incoherent J/ψ, photon-photon, and J/ψ gun samples.

The probe is then checked. If it meets the criteria of a passing probe that pair is marked as passing. The pairs with, passing probes, failing probes, and all probes are plotted and fit. The three sets of pairs are fit using a simultaneous fit for the signal with the failing and passing background shapes left independent. The signal yields have to be consistent between the three sets of pairs. The number of signal passing pairs and failing pairs is forced to equal the number of total pairs.

To measure the trigger efficiency a tag is required to pass all muon quality cuts and matched to the trigger. The probe is required to pass all quality cuts. A passing probe is a probe that is

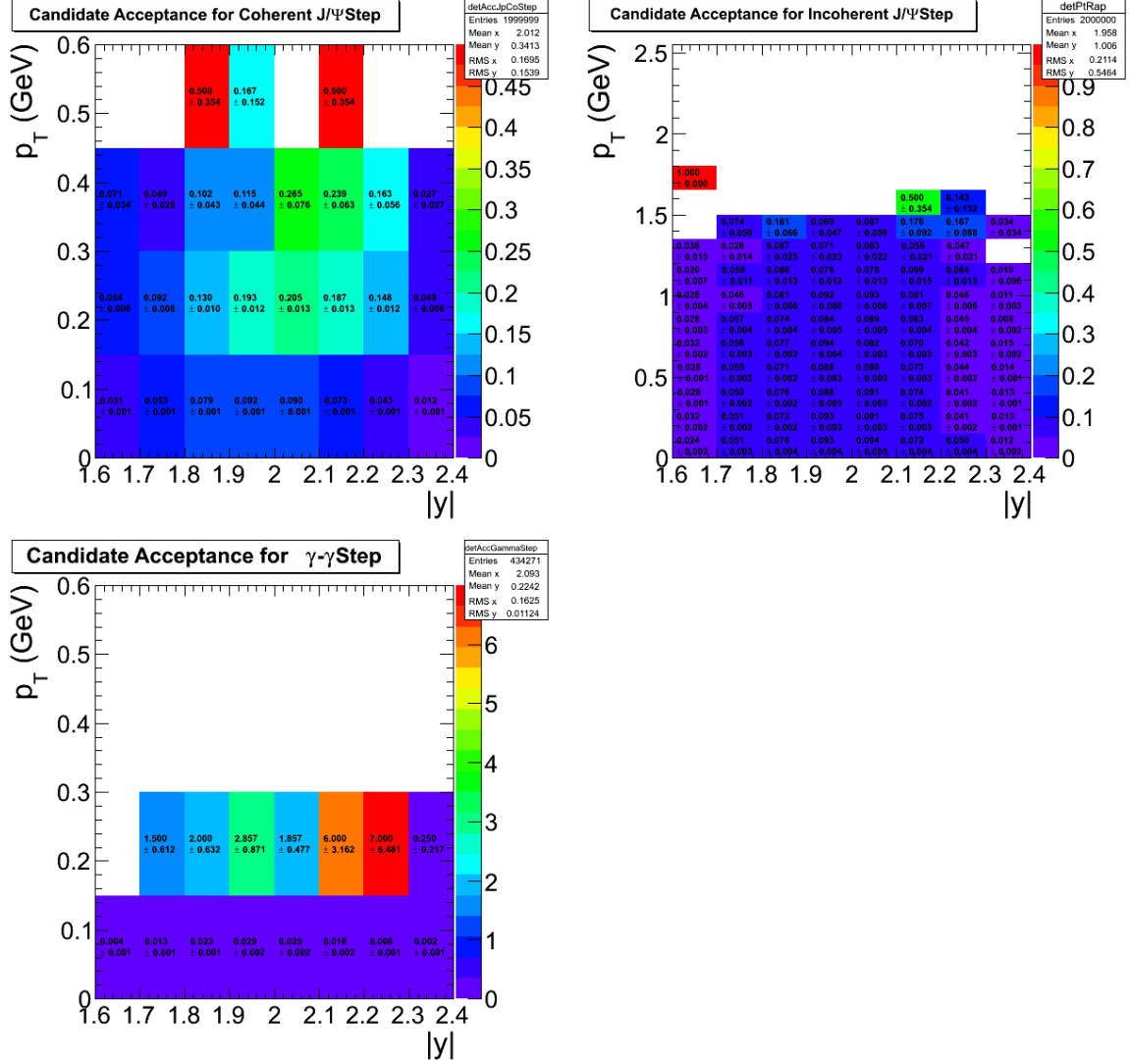


Figure 4.13: Dimuon acceptance from coherent  $J/\psi$  (top left), incoherent  $J/\psi$  (top right), and photon-photon interactions (lower).

also matched to the trigger. In this way the tag leaves the probe in biased by the trigger and the efficiency can be measured by fitting mass.

Fig. 4.14 shows the fit of the three sets of pairs. This fit is done for each bin of the probes  $p_T$  and  $\eta$ . The resulting fit is in Fig. 4.15.

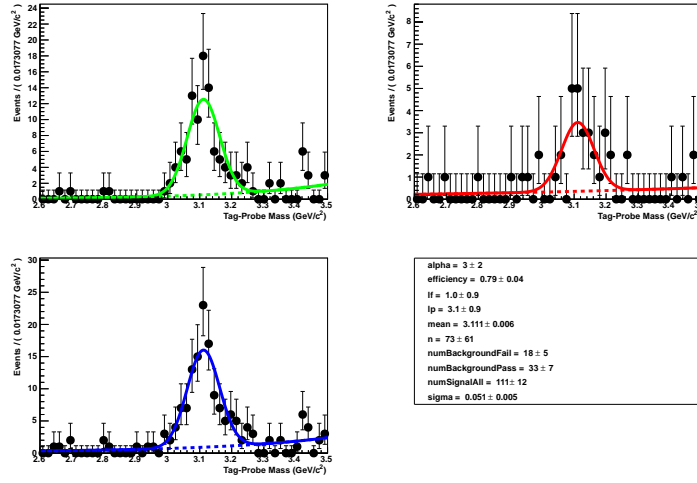


Figure 4.14: Fits to tag and probe pairs in the  $J/\psi$  mass region.

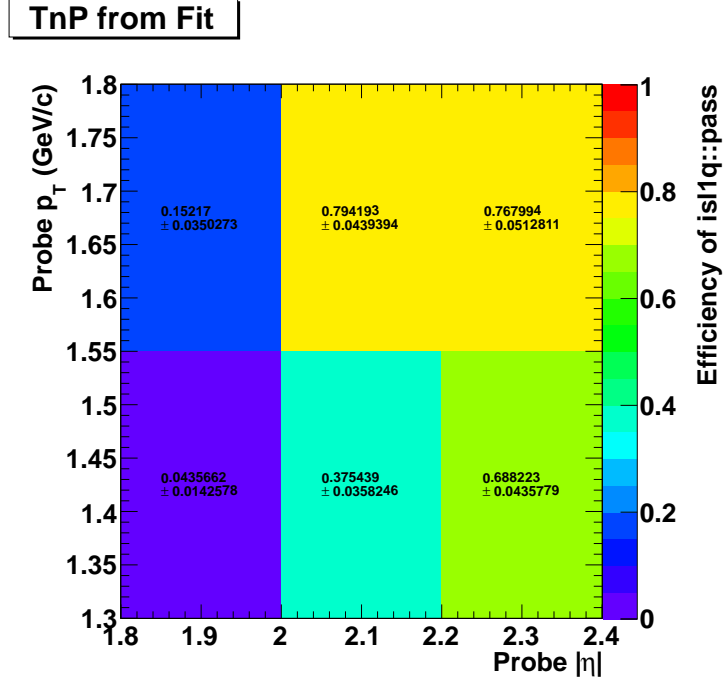


Figure 4.15: Muon trigger efficiencies in  $p_T$  and  $\eta$  bins from the tag and probe method.

# Chapter 5

## Results

### 5.1 Coherent cross section

### 5.2 Incoherent cross section

### 5.3 Break up ratios

### 5.4 diMuon-neutron correlations

The invariant mass distribution for different break-up modes is show for the coherent and incoherent  $J/\psi$  on the Fig. 5.1 and Fig. 5.2 respectively.

The number of the coherent and incoherent  $J/\psi$  for each break-up mode are given in the Tab. 5.1. The ratios between the modes  $X_n X_n$ ,  $1_n 0_n$ ,  $1_n 1_n$  and the mode  $X_n 0_n$  are given in the table Tab. 5.2. Some of the ratios can be obtained from STARLIGHT and from the Zhalov and thus are given in Tab. 5.3.

For statistical reason, further studies concentrate only on the break-up mode  $X_n 0_n$ . Figure 5.5 shows the transverse momentum distribution of the  $J/\psi$  (coherent and incoherent) in the case when  $J/\psi$  and neutron have the same or opposite rapidity direction. The ratio between



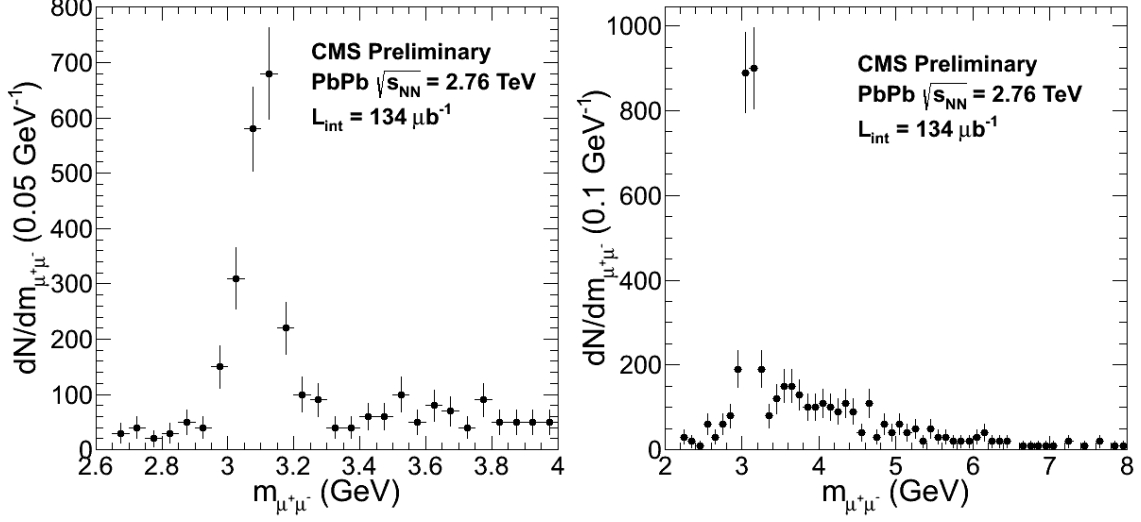


Figure 5.1: Invariant mass spectrum of the opposite signs di-muons originating from the coherent  $J/\psi$  for  $X_n 0_n$  breakup mode for two invariant mass regions.

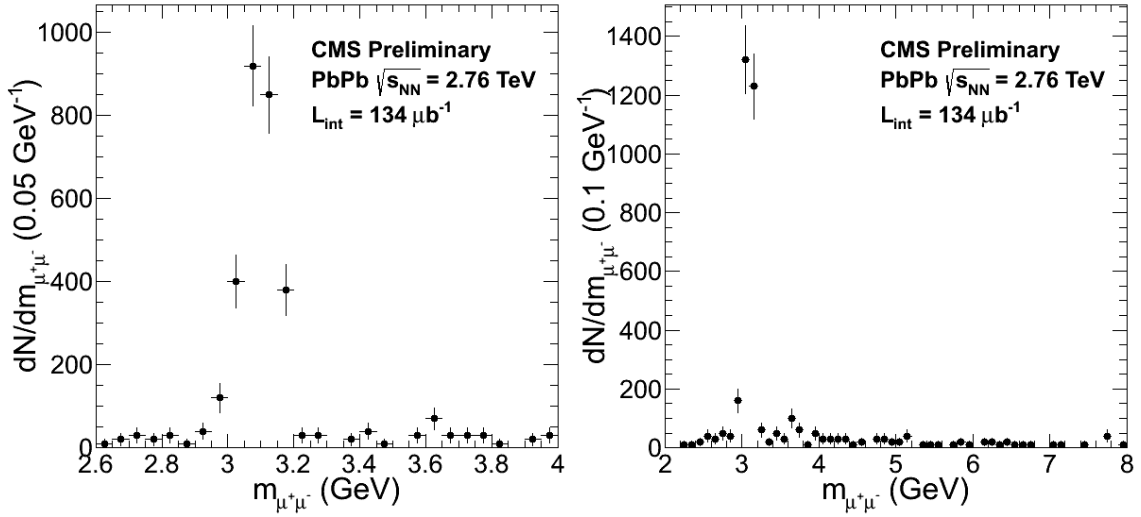


Figure 5.2: Invariant mass spectrum of the opposite signs di-muons originating from the incoherent  $J/\psi$  for  $X_n 0_n$  breakup mode for two invariant mass regions.

the  $J/\psi$  and neutron that have the opposite direction and the  $J/\psi$  and neutron that have the same direction is shown on Fig. 5.6. The red curve gives the pure theory calculations, the black one gives the theory results that are injected to the detector simulation and thus taking into account experimental bias.

The rapidity distributions of the coherent and incoherent  $J/\psi$  are shown in the Fig. 5.7. They

Table 5.1: Number of coherent  $J/\psi$  integrated over  $p_T$  and  $y$  with statistical uncertainty.

	$X_n 0_n$	$X_n X_n$	$1_n 0_n$	$1_n 1_n$
coherent $J/\psi$	$242 \pm 16$	$94 \pm 10$	$58 \pm 8$	$8 \pm 3$
incoherent $J/\psi$	$291 \pm 17$	$57 \pm 8$	$19 \pm 4$	$2 \pm 1$

Table 5.2: Number of coherent  $J/\psi$  integrated over  $p_T$  and  $y$  with statistical uncertainty.

	$X_n X_n / X_n 0_n$	$1_n 0_n / X_n 0_n$	$1_n 1_n / X_n 0_n$
coherent $J/\psi$	$0.39 \pm 0.05$	$0.24 \pm 0.04$	$0.03 \pm 0.01$
incoherent $J/\psi$	$0.20 \pm 0.03$	$0.07 \pm 0.02$	$0.007 \pm 0.005$

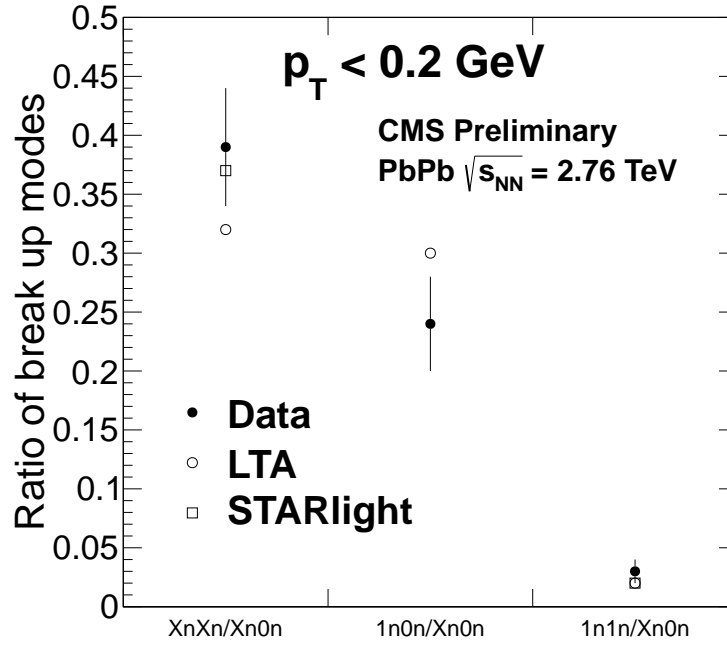


Figure 5.3: Ratio between  $J/\psi$  yields  $X_n X_n$  and  $1_n 0_n$  break-up modes compared the  $X_n 0_n$  break-up mode for  $J/\psi$  with  $p_T$  below 150 MeV.

are shown separately for the events firing the  $ZDC^+$  and  $ZDC^-$ . The same distributions are also obtained for the MC and shown in Fig. 5.8. For the MC the particle gun generator with the input  $p_T$  spectrum from Zhalov's calculation (LTA). The rapidity symmetry for coherent  $J/\psi$  and asymmetry for incoherent  $J/\psi$  are observed in data and MC. These are quantified in the Tab. 5.4.

Table 5.4 gives the number of coherent and incoherent  $J/\psi$  separately for the events that fired

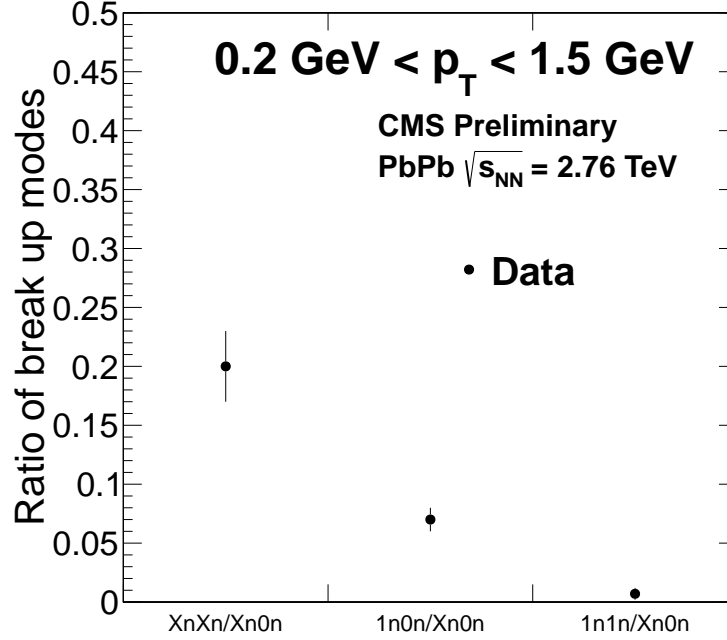


Figure 5.4: Ratio between  $J/\psi$  yeilds  $X_nX_n$  and  $1n0n$  break-up modes compared the  $X_n0n$  break-up mode for  $J/\psi$  with  $0.2 < p_T < 1.5$  GeV.

Table 5.3: Number of  $J/\psi$  integrated over  $p_T$  and  $y$  with statistical uncertainty.

	$X_nX_n/X_n0_n$	$1_n0_n/X_n0_n$	$1_n1_n/X_n0_n$
STARlight coherent	0.37	-	0.02
Zhalov coherent	0.32	0.30	0.02
STARlight incoherent	0.37	-	$0.007 \pm 0.02$

the  $ZDC^-$  and  $ZDC^+$ . We quote separately the  $J/\psi$  that have the same or opposite rapidity direction to the neutron direction. The ratios, as described below are also given in the Tab. 5.4:  $R_{ZDC^-}^{y^+/y^-}$  : ratio between the number of  $J/\psi$  having  $y > 0$  to the number of  $J/\psi$  having  $y < 0$  from the events that fired  $ZDC^-$

$R_{ZDC^+}^{y^-/y^+}$  : ratio between the number of  $J/\psi$  having  $y < 0$  to the number of  $J/\psi$  having  $y > 0$  from the events that fired  $ZDC^+$

The combined ratio  $R_{opp/same}^c$  is calculated as

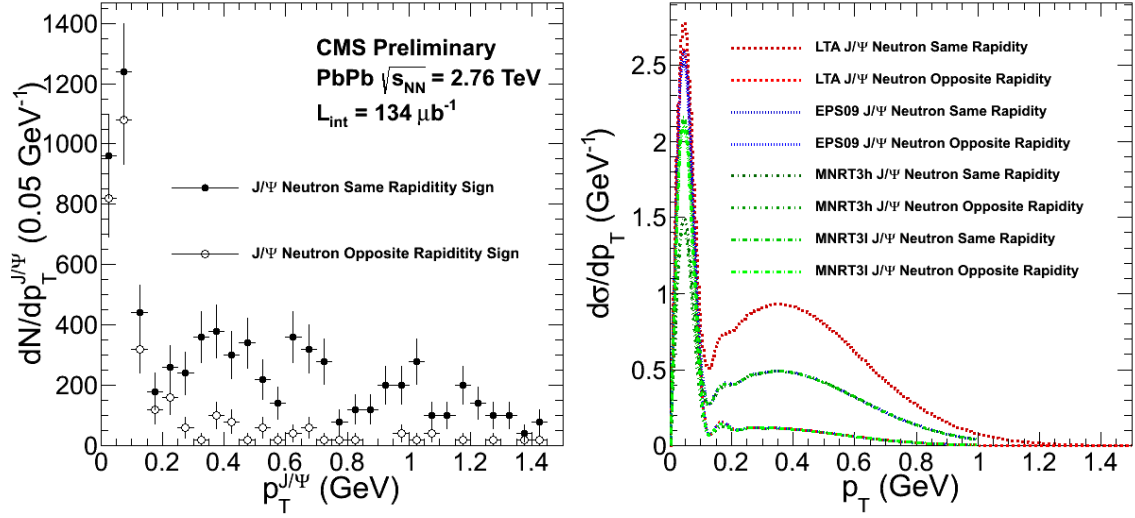


Figure 5.5: Transverse momentum distribution of the  $J/\psi$  when  $J/\psi$  and neutron have the same or opposite rapidity direction from data (left) and from theory (right).

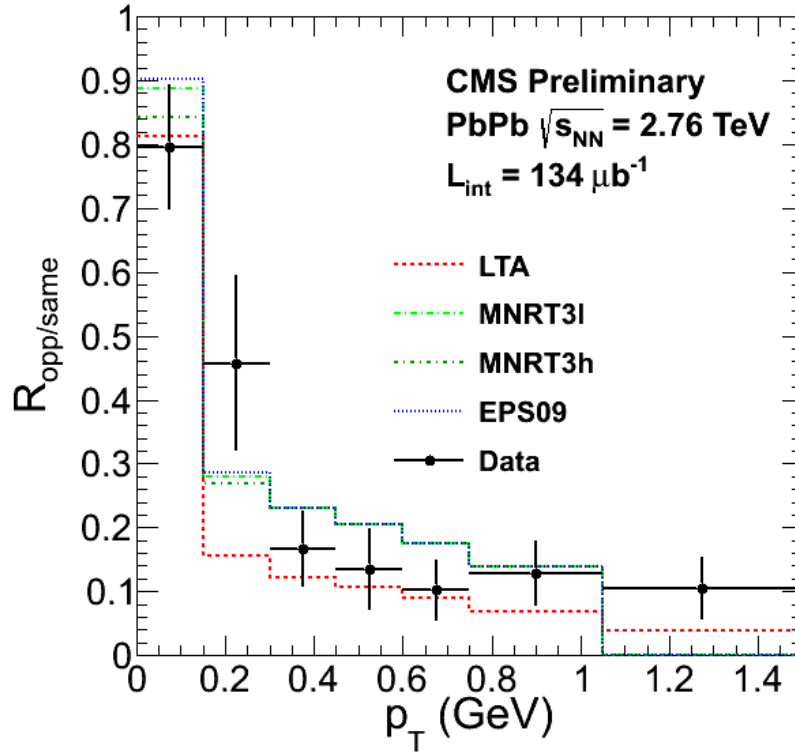


Figure 5.6: Ratio between the transverse momentum distribution of the  $J/\psi$  when  $J/\psi$  and neutron have the opposite direction and the transverse momentum distribution of the  $J/\psi$  when  $J/\psi$  and neutron have the same direction.

Table 5.4: Final number of  $J/\psi$  (for both ZDCs and for two negative and positive rapidity) and ratios with statistical uncertainty.

	ZDC <sup>-</sup> $y < 0$	ZDC <sup>-</sup> $y > 0$	$R_{ZDC^-}^{y^+/y^-}$	ZDC <sup>+</sup> $y < 0$	ZDC <sup>+</sup> $y > 0$	$R_{ZDC^+}^{y^-/y^+}$
coherent $J/\psi$	63	68	$1.08 \pm 0.19$	42	69	$0.61 \pm 0.12$
incoherent $J/\psi$	141	26	$0.184 \pm 0.039$	13	111	$0.117 \pm 0.034$

$$R_{opp/same}^c = \frac{ZDC^- \text{ and } y > 0 + ZDC^+ \text{ and } y < 0}{ZDC^- \text{ and } y < 0 + ZDC^+ \text{ and } y > 0}$$

- $R_{opp/same}^c$  for coherent  $J/\psi = 0.83 \pm 0.12$ .
- $R_{opp/same}^c$  for incoherent  $J/\psi = 0.155 \pm 0.021$ .

The correction factors (efficiency, reconstruction) are as following:

- $\epsilon_{ZDC^-}$ : efficiency of the ZDC<sup>-</sup> of 0.98
- $\epsilon_{ZDC^+}$ : efficiency of the ZDC<sup>+</sup> of 0.94
- $\epsilon_{\mu^-}$ : efficiency  $\times$  reconstruction of the muons with rapidly  $< 0$ : 1.0
- $\epsilon_{\mu^+}$ : efficiency  $\times$  reconstruction of the muons with rapidly  $> 0$ : 1.014.

The combined ratio  $R_{opp/same}^{eff}$  corrected with the factors above is calculated as

$$R_{opp/same}^{eff} = \frac{\epsilon_{ZDC^-} \epsilon_{\mu^+} ZDC^- \text{ and } y > 0 + \epsilon_{ZDC^+} \epsilon_{\mu^-} ZDC^+ \text{ and } y < 0}{\epsilon_{ZDC^-} \epsilon_{\mu^-} ZDC^- \text{ and } y < 0 + \epsilon_{ZDC^+} \epsilon_{\mu^+} ZDC^+ \text{ and } y > 0}$$

$R_{opp/same}^{eff}$  is  $0.83 \pm 0.12$ .

- $R_{opp/same}^{eff}$  for coherent  $J/\psi = 0.83 \pm 0.12$ .

- $R_{opp/same}^{eff}$  for incoherent  $J/\psi = 0.154 \pm 0.021$ .

If considering 3 significant figures for the representation of the result these values are:

- $R_{opp/same}^c$  for coherent  $J/\psi = 0.833 \pm 0.124$
- $R_{opp/same}^c$  for incoherent  $J/\psi = 0.155 \pm 0.021$
- $R_{opp/same}^{eff}$  for coherent  $J/\psi = 0.828 \pm 0.124$
- $R_{opp/same}^{eff}$  for incoherent  $J/\psi = 0.154 \pm 0.021$

This shows that in this measurement the efficiencies factors are negligible.

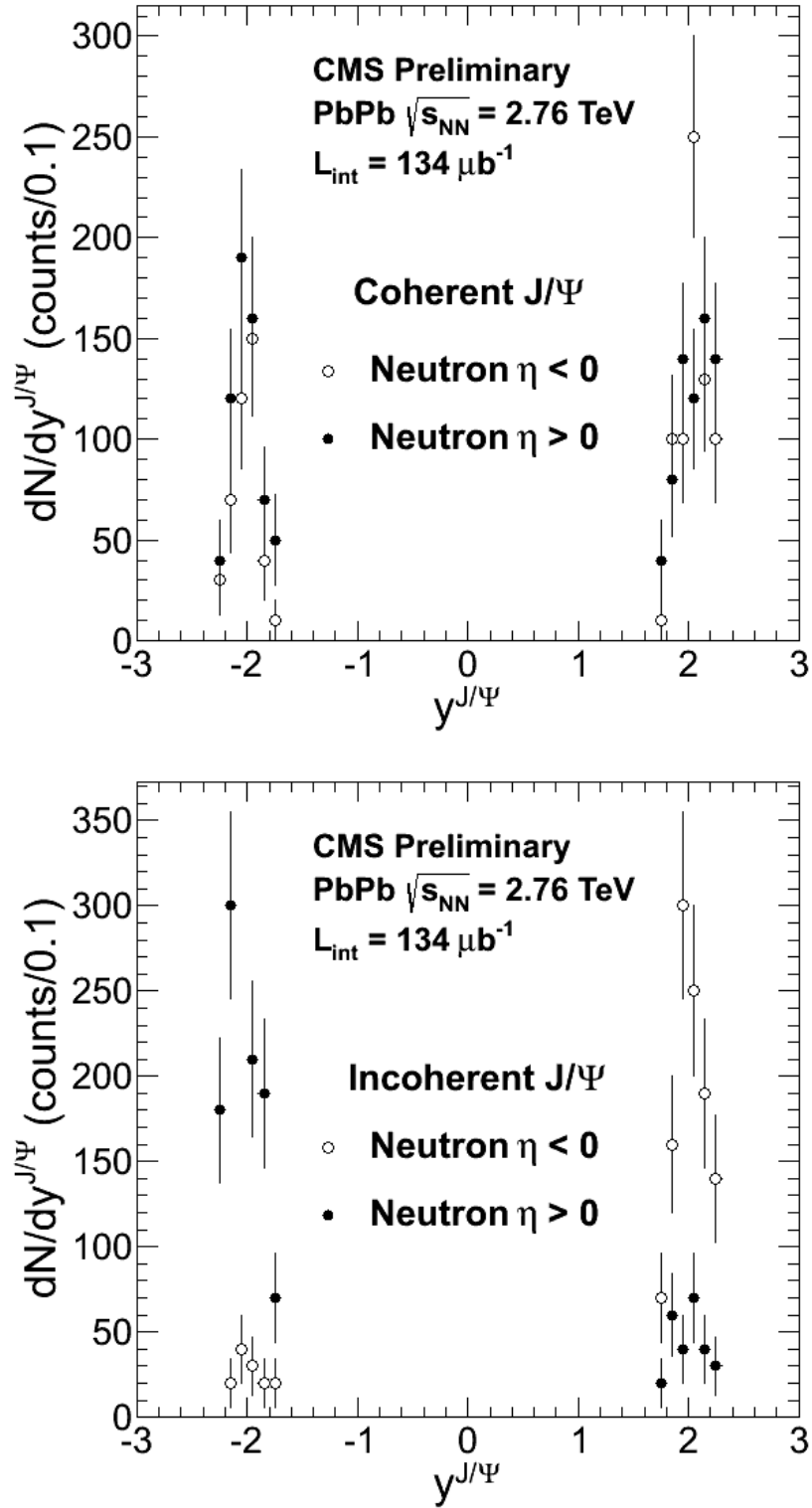


Figure 5.7: The rapidity distribution of the coherent (top) and incoherent (bottom)  $J/\psi$  for the  $ZDC^+$  and  $ZDC^-$ .

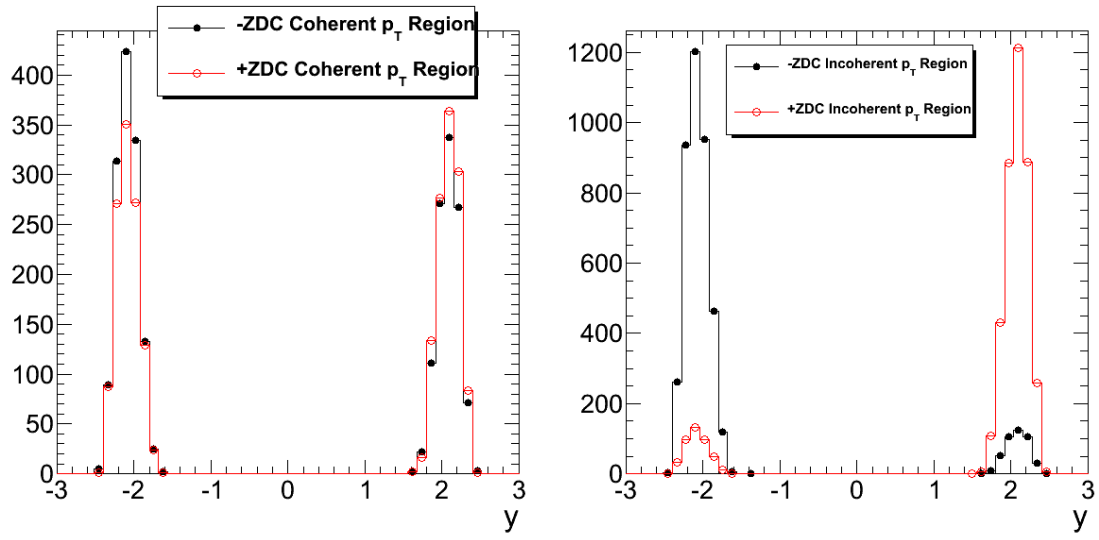


Figure 5.8: The rapidity distribution of the coherent (left) and incoherent (right)  $J/\psi$  for the  $ZDC^+$  and  $ZDC^-$  from MC (particle gun with customized  $J/\psi p_T$  input distribution).



# **Chapter 6**

## **Conclusion**

### **6.1 xsection results**

### **6.2 correlation results**

# Chapter 7

## Future Works

### 7.1 Studies of 2011 PbPb data

#### 7.1.1 High mass $\gamma - \gamma \rightarrow e^+ e^-$ in PbPb 2011

A study of the di-electron production in UPC events is already possible from the recorded 2011 data. This measurement would make use of the electron triggers and combined the current di-muon data with di-electron data from the triggers using the ECAL. The electron triggered sample potentially offers a large increase in statistics. By adding the additional channel the statistics would already increase. However in addition to this, because of the smaller mass of the electron, di-electron production is slightly favor compared to di-muon production. STARlight predicts that di-electron cross section is a factor of more than 2.5 higher in Xn break-up mode than the di-muons channel when looking at masses above 4 GeV. The acceptance for electrons is potential higher as well. The ECAL is position just beyond the tracker, whereas the muon system is outermost sub-detector. This elevates the main reduction of muon acceptance, which is the material budget. There is simply a lot a detector in front the muon system.

In order to perform the study several key additions would need to be made relative to the current di-muon analysis. The original reconstruction of the data used in the current di-muon analysis does not contain electron objects. Either the analysis would have to migrated to reconstruction of the

data done in a newer software version, or reconstruction of the electrons would have to be added to the current analysis chain. There are currently no electron UPC MC samples produced. In order to study the acceptance and efficiency for electrons these samples would be needed. The ultimate limitation on this study is the 2 GeV threshold in  $p_T$  in the ECAL trigger. This limits the di-electron mass range to where the trigger is efficient.

The contribution of higher order diagrams can be explored by the photoproduction of di-lepton pairs is to explore. With additional contributions to the physics communities understanding of this process this study will help to determine necessity or non-necessity of including higher order of corrections in simulations such as STARlight. Having an additional channel to help constrain the current di-muon measure of the of UPC  $\gamma - \gamma$  interaction will also help to constrain the  $J/\psi$  measurement by adding a data driven check on the normalization  $\gamma - \gamma$  background to the  $J/\psi$

### 7.1.2 UPC Hadronic Overlap and PbPb 2011

In the model calculations explored in this analysis of UPC quarkonia photoproduction all hadronic interactions are rejected. Photoproduction in events where hadronic interactions occur are not included in the cross section calculation. However, inclusive  $p_T$  spectra of  $J/\psi$  measured by ALICE in peripheral PbPb collisions show a low momentum peak consistent with coherent photoproduction [13]. CMS has the opportunity to explore this overlap between hadronic interactions and photoproduction using PbPb data from 2011 that is already recorded.

To study the overlap between photoproduction and hadronic production of quarkonia event the inelastic sample and the UPC sample could both be used. The looseness of the veto designed to reject hadronic interactions, which uses the BSC detector, leaves a significant overlap with peripheral hadronic collisions. The inclusive quarkonia sample from typical hadronic collisions can also be utilized. Coherent quarkonia photoproduction has a distinctive low  $p_T$  structure that can be used to identify photoproduced candidates in a sample that contains photoproduction combined with hadronic interactions. This measurement would open up the door to exploring the boundary between photoproduction and hadronic production. By looking at the mixing of the two, both

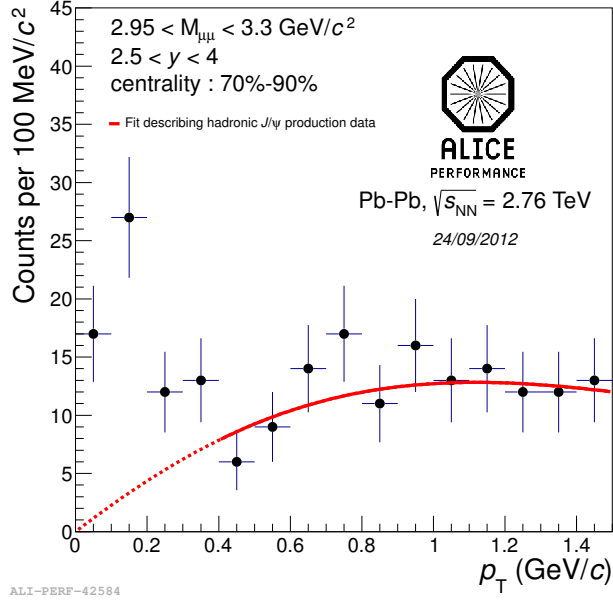


Figure 7.1: Coherent excess in inclusive  $J/\psi$   $p_T$  spectrum.

process, hadronic production and photoproduction, will be better understood.

In order to compliment each others strengths, the inclusive hadronic sample and the UPC sample of dimuon candidates would be utilized in this study. The two samples muon and centrality biases are orthogonal allowing each to serve as a check on the other. The inclusive hadronic sample is triggered by a higher  $p_T$  threshold double trigger, whereas the UPC sample is uses a lower  $p_T$  single muon trigger. The UPC sample is strongly biased toward peripheral events, which would lead to inefficiencies as events become more central, whereas, the inclusive sample is slightly biased in the most peripheral events due to an inefficiency an event selection efficiency in the most peripheral centrality bin. If these offsetting biases can be exploited, clarity about the transition between and mixing of photoproduction and hadronic production of quarkonia can be produced. A measurement of the kind proposed here will both produce a better understanding of the low  $p_T$  portion of the inclusive spectrum as well as the hadronic overlap with UPC measurements.

### 7.1.3 UPC with muons in HF

As higher rapidities are explored both lower and higher momentum partons of the nucleus are probed. Because these two contributions to the UPC photoproduction cross section can be separated using neutron tagging in incoherent events, exploring higher dimuon rapidities becomes attractive. HF extends to 5 in  $\eta$ , 2.6 units beyond the edge of the tracker. By combining hits in HF with tracks in the tracker the higher dimuon rapidities could be explored. When combined with neutron tagging of incoherently produced quarkonia, the current study can be extended to probe lower- $x$  nuclear partons by identifying muons in HF.

## 7.2 Studies of 2013 pPb data and 2015 PbPb data

Specific UPC triggers were also developed for the pPb run in 2013. For this period of running a much higher total trigger rate was read out relative to 2011. The total rate allocated for UPC triggers at the L1 in 2013 was 5kHz and 50 Hz at the HLT. This factor of 5 increase in the bandwidth, especial in L1 rate, allowed for a different triggering strategy than in 2011.

The basic strategy in 2013 was the same as in 2012, use the loosest available ECAL and muon L1 triggers to push to capture the lowest  $p_T$  electrons and muons possible paired with a veto on hadronic interactions, but was implemented differently. Because of the L1 bandwidth restrictions in 2011, both the ZDC and the BCS were used on the L1 to reduce rates. In 2013 only the muon and ECAL triggers were used on the L1 allowing for rejection of hadronic interactions through cuts on track multiplicity. In addition, a more sophisticated trigger using full dimuon reconstructed was developed to increase purity. The main advantage in this shift in strategy was a higher purity due to the increased sophistication of the reconstruction on the HLT. In addition, an increase in cross section of the underlying physics process was achieved by relaxing the neutron emission requirement.

The PbPb run in 2015 will be at higher beam energies and luminosities. The  $\sqrt{s_{NN}}$  will increase from 2.76 TeV in 2011 to 5.1 TeV with a project integrated luminosity between 0.3/nb

and  $1/nb$ . The factor of 2 to 10 increase in integrated luminosity will increase the number of events directly. In addition, both the increase in energy, which increases the photon flux, and the ability to utilize the 2013 trigger strategy of sifting the onus of the trigger selection to the HLT will increase the measured yields relative to 2011. The higher beam energy, higher integrated luminosity, and added selectivity of the HLT will create the opportunity to explore both  $J/\psi$  with greater statistical precision and novel objects such as  $\Upsilon$ , and jets.

### 7.2.1 pPb $J/\psi$

$J/\psi$  photoproduction in pPb collisions is dominated  $\gamma - p$  interactions. The measurement would primarily probe the proton gluon densities. In Eq. 2.13 the photon flux depends on the square of the number of protons in parent nucleus,  $Z^2$ . However, the cross section of the target only increase as the total number of nucleons to the 2/3rds power,  $A^{2/3}$ . The much higher photon flux from the Pb ion more than compensates for the decreased size of the proton.

A pPb UPC  $J/\psi$  measurement will compliment the measurements done at HERA, and measurements done by ALICE. CMS will contribute by adding additional kinematic coverage and cover a unique range of proton-photon center of mass energies,  $W_{p\gamma}$ . The difference in beam energies and species at LHC versus HERA result in access to different  $W_{p\gamma}$ . ALICE and CMS have different acceptance in  $J/\psi$  rapidity, which also translates to coverage of different  $W_{p\gamma}$ . In addition, an excess in the UPC cross section compared to HERA measurements would indicate a non-exclusive contribution to the pPb UPC  $J/\psi$  cross section. This measurement will both help enhance the current understanding of the  $p\gamma J/\psi$  photoproduction cross section as a function of  $W_{p\gamma}$ , and validate the UPCs measurements as an extension of the work done at HERA.

### 7.2.2 UPC $J/\psi$ and $\Upsilon$ in 2015

A measurement of the UPC  $J/\psi$  in 2015 will produce a strong constraint on the low-x portion of the nuclear gluon distribution relative to the current analysis from the 2011 data. The  $J/\psi$  measurement will probe lower-x than in 2011 due to the increase in beam energy. A measurement

in 2015 will also have lower statistical errors due to the increase in integrated luminosity and increased L1 bandwidth. UPC  $J/\psi$ s in 2015 will push farther towards the onset of low- $x$  parton saturation.

Measurement of the UPC  $\Upsilon$  cross section from the 2015 data will be the first from PbPb collisions. As with the  $J/\psi$ , Additional L1 bandwidth, increased beam energy, and and intensity will increase the  $\Upsilon$  yield significantly relative to 2011. CMS's acceptance for  $\Upsilon$  is far higher than for  $J/\psi$ . The acceptance for  $\Upsilon$  is near 40% for all rapidities between -2.4 to 2.4. Conversely,  $J/\psi$  acceptance is 8% near 2 in dimuon rapidity only. Below 1.6 in rapidity there is not acceptance for for UPC  $J/\psi$ . Estimates from STARlight predict a factor of 17-60 increase in yield depending on the total delivered integrated luminosity. The  $\Upsilon$  measurement will be a new measurement that will expand the range of  $x$  and  $Q^2$  probed with a higher energy probe that is better suited to the acceptance of CMS.

### 7.2.3 UPC jets

Like  $\Upsilon$ s, UPC photoproduction of jets is a novel probe. The LHC 2015 heavy ion run presents an opportunity do this measurement for the first time. The cross section for photoproduction of jets was estimated in Ref [?] and found  $b\bar{b}$  and  $c\bar{c}$  on the order of 1 mb and 1b respectively. With the integrated luminosity expected for 2015 as many as  $1 \times 10^6$   $b\bar{b}$  events and  $1 \times 10^9$   $c\bar{c}$  events. Jet photoproduction is not constrained by the mass of the bound onia states like in  $J/\psi$  and  $\Upsilon$  photoproduction. For this reason, jet photoproduction probes a wider range of  $x$  and  $Q^2$ . UPC jets therefore will both expand on the  $J/\psi$  and  $\Upsilon$  measurements in addition to providing an additional validating compliment to the onia measurements.

The jet measurement will require additional trigger development and analysis design. The jet signal differs significantly from the dimuon signals used in the current analysis. The trigger scheme used in the 2013 pPb run selected UPC events by vetoing events with high numbers of track. The track multiplicity of the jets will not pass this requirement. However, new L1 trigger logic is currently being developed to separate the jet from the underlying event in nuclear collisions. This

trigger logic could also be utilized to select jet events that produce very little to no underlying event. In addition to the trigger, jet reconstruction algorithms would need to be adapted to push to the lower  $p_T$  jets they are produced by photoproduction. The UPC jet measurement will demand extra preparation compared to the onia measurements, but the development will overlap with many of the goals that are already being pursued by the CMS Heavy Ion group and will allow for wider collaboration.



# References

- [1] S. Chatrchyan *et al.*, “The cms experiment at the cern lhc,” *Journal of Instrumentation* **3** no. 08, (2008) S08004. <http://stacks.iop.org/1748-0221/3/i=08/a=S08004>.
- [2] **PHENIX Collaboration** Collaboration, A. Adare *et al.*, “Cold Nuclear Matter Effects on  $J/\psi$  Yields as a Function of Rapidity and Nuclear Geometry in Deuteron-Gold Collisions at  $\sqrt{s_{NN}} = 200$  GeV,” *Phys.Rev.Lett.* **107** (2011) 142301, [arXiv:1010.1246](https://arxiv.org/abs/1010.1246) [nucl-ex].
- [3] J. D. Jackson, *Classical electrodynamics*. Wiley, New York, NY, 3rd ed. ed., 1999. <http://cdsweb.cern.ch/record/490457>.
- [4] E. Fermi, “On the Theory of Collisions between Atoms and Electrically Charged Particles,” in *Electromagnetic Probes of Fundamental Physics*, W. Marciano and S. White, eds., pp. 243–252. Sept., 2003. [hep-th/0205086](https://arxiv.org/abs/hep-th/0205086).
- [5] C. A. Brau, *Modern Problems in Classical Electrodynamics*. Oxford, New York, NY, 1st ed. ed., 2004.
- [6] S. R. Klein and J. Nystrand, “Exclusive vector meson production in relativistic heavy ion collisions,” *Phys. Rev. C* **60** (Jun, 1999) 014903. <http://link.aps.org/doi/10.1103/PhysRevC.60.014903>.
- [7] V. Rebyakova, M. Strikman, and M. Zhalov, “Coherent rho and J/psi photoproduction in ultraperipheral processes with electromagnetic dissociation of heavy ions at RHIC and LHC,” *Phys.Lett.* **B710** (2012) 647–653, [arXiv:1109.0737](https://arxiv.org/abs/1109.0737) [hep-ph].

- [8] V. Rebyakova, M. Strikman, and M. Zhalov, “Coherent  $\rho$  and  $J/\Psi$  photoproduction in ultraperipheral processes with electromagnetic dissociation of heavy ions at RHIC and LHC,” *Physics Letters B* **710** no. 4–5, (2012) 647 – 653.  
<http://www.sciencedirect.com/science/article/pii/S0370269312003152>.
- [9] A. Adeluyi and C. A. Bertulani, “Gluon distributions in nuclei probed at energies available at the CERN large hadron collider,” *Phys. Rev. C* **84** (Aug, 2011) 024916.  
<http://link.aps.org/doi/10.1103/PhysRevC.84.024916>.
- [10] A. Adeluyi and T. Nguyen, “Coherent photoproduction of  $\psi$  and  $\Upsilon$  mesons in ultraperipheral pPb and PbPb collisions at the CERN Large Hadron Collider at  $\sqrt{s_{NN}} = 5$  TeV and  $\sqrt{s_{NN}} = 2.76$  TeV,” *Phys. Rev. C* **87** (Feb, 2013) 027901, arXiv:1302.4288 [nucl-th]. <http://link.aps.org/doi/10.1103/PhysRevC.87.027901>.
- [11] **ALICE** Collaboration, B. Abelev *et al.*, “Coherent  $J/\psi$  photoproduction in ultra-peripheral Pb-Pb collisions at  $\sqrt{s_{NN}} = 2.76$  TeV,” *Physics Letters B* **718** no. 4–5, (2013) 1273 – 1283.  
<http://www.sciencedirect.com/science/article/pii/S0370269312012257>.
- [12] V. Guzey, E. Kryshen, M. Strikman, and M. Zhalov, “Evidence for nuclear gluon shadowing from the ALICE measurements of pPb ultraperipheral exclusive production,” *Physics Letters B* **726** no. 1–3, (2013) 290 – 295.  
<http://www.sciencedirect.com/science/article/pii/S0370269313006825>.
- [13] A. Lardeux, “ $J/\psi$  production in Pb-Pb collisions at  $\sqrt{s_{NN}} = 2.76$  TeV in the ALICE experiment,” *J.Phys.Conf.Ser.* **446** (2013) 012042.

# **Appendix A**

## **My Appendix, Next to my Spleen**

There could be lots of stuff here